NTNU – Trondheim
Norwegian University of
Science and Technology

Gold and Platinum Surface Nanostructures on Highly Oriented Pyrolytic Graphite

Terje Kultom Karlsen

Master of Science in Physics and Mathematics
Submission date: June 2012
Supervisor: Steinar Raaen, IFY
Co-supervisor: Armen Julukian, IFY

Norwegian University of Science and Technology
Department of Physics

Gold and Platinum Surface Nanostructures on Highly Oriented Pyrolytic Graphite

Terje Kultom Karlsen

Trondheim, 13. juni 2012

Abstract

Self-assembled platinum and gold nanostructures, which are formed by evaporation and subsequent diffusion limited aggregation of metal on highly oriented pyrolytic graphite, have been studied by photoemission spectroscopy and scanning electron microscopy. Dendritic gold nanostructures were observed on samples onto which gold was evaporated at room temperature. For samples onto which gold was evaporated at reduced temperatures, no such dendrites were found. For samples evaporated with platinum, small nano-spiders were seen at low evaporation time, and more complex fractal structures at higher evaporation time. Studying the oxidation of carbon monoxide over the platinum nanostructures yielded no clear corrolation between nanostructure size and oxidation rate.

Sammendrag

Selvsammensatte nanostrukturer av platina og gull, som har blitt formet ved pådamping og påfølgende diffusjonsbegrenset aggregering av metall på høyorientert pyrolytisk grafitt, har blitt studert ved hjelp av fotoemmisjonsspektroskopi og sveipeelektronmikroskopi. Dendritiske nanostrukturer av gull ble observert på prøver som ble pådampet med gull ved romtemperatur. For prøver hvor gull ble pådampet ved lavere temperaturer, ble ingen dendritter funnet. For prøver som ble pådampet med platina ble nano-spiders" observert ved kort pådampingstid, og mer komplekse fraktaler ved lengre pådampingstid. Studier av oksidering av karbonmonoksid over nanostrukturene av platina viste ingen korrelasjon mellom størrelsen på strukturene og oksidasjonsraten.

Foreword

This master thesis is a continuation of my project work from the fall of 2011.

I would like to thank my supervisors prof. Steinar Raaen and PhD candidate Armen Julukian for guidance throughout the entire project process. I would also like to thank David Franke for help with the SEM imaging.

Contents

Chapter 1

Introduction

The properties of metals change to various degrees when their size is reduced to the nanometer scale. The change in these properties can for example lead to significant changes in catalytic processes. A nanoparticle array contains new degree of freedom that affect the reaction output. These are particle size and shape, and the interaction between the particles and the substrate [1].

The aim of this thesis is to study two-dimensional metal nanoparticle systems in order to obtain knowledge to contibute to the understanding of the complex phenomena taking place in such systems.

Focus is put on the growth of gold and platinum nanostructures on HOPG formed by evaporation and subsequent diffusion limited aggregation on the surface.

Chapter 2

Theory

2.1 Materials

2.1.1 Highly Oriented Pyrolytic Graphite (HOPG)

Carbon has atomic number 6, and the electronic configuration [He]$2s^2 2p^2$ [2]. Figure 2.1 shows the hexagonal crystal structure of graphite with lattice constants of 2.4612 Å within the graphene layer and 6.709 Å between two repeating graphene layers. In highly ordered pyrolytic graphite, the crystal structure excibits a high degree of order. This means that the surface of the graphite will form an area which is flat on an atomic scale. The graphite also forms an inert surface.

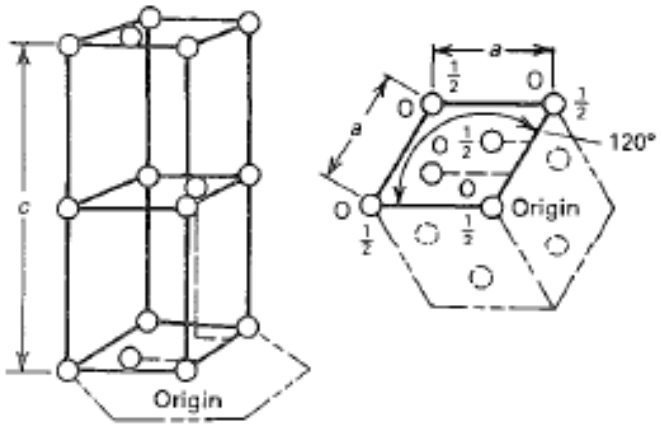

Figure 2.1: The hexagonal lattice structure of graphite (a = 2.4612 Å, c = 6.709 Å)[3]

.

2.1.2 Gold

Gold is a highly malleable and ductile transition metal with atomic number 79. Its electronic configuration is $[Xe]4f^{14}5d^{10}6s^1$ [2]. Figure 2.2 shows the FCC* crystal structure of gold with a lattice constant of 4.0782 Å [3]. Solid gold is inert and does not readily react with anything. A solid gold surface is not catalytically active at extended surfaces.

Gold nanoparticles Whereas solid gold is very chemically stable and catalytically inert, nano-sized gold particles are catalytically active. Nanoparticles of gold can catalyze CO oxidation at room temperature and below, which is significally lower temperatures than those required using more traditonal supported metal catalysts. This lower temperature dependence holds true for a number of catalytic reactions. Better control over these catalytic reactions will lead to reduced operating cost, and can increase the selectivity of the reactions, leading to cleaner reactions. Gold catalysts may have a future in cleaning exhaust, since low reaction temperature is a must[4].

2.1.3 Platinum

Platinum is a malleable and ductile transition metal with atomic number 78. Its electronic configuration is $[Xe]4f^{14}5d^{9}6s^1$ [2]. Figure 2.2 shows the FCC crystal structure of platinum with a lattice constant of 3.9236 Å [3]. Platinum is not very reactive and is very resistant to atmospheric corrosion at normal temperatures.

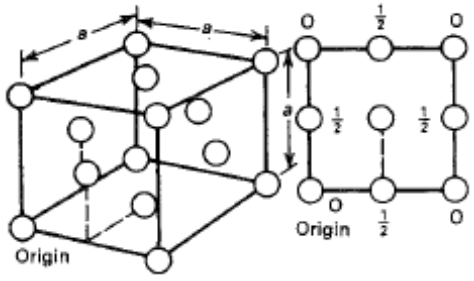

Figure 2.2: The FCC lattice structure of gold ($a = 4.0782$ Å) and platinum ($a = 3.9236$ Å)[3]

.

*Face centered cubic

Platinum nanoparticles Platinum nanoparticles keep the catalytic properties of the solid metal, and the added degrees of freedom created by nano-sized particles can enhance or change these properties. Desorption of carbon monoxide gas from platinum nanostructures occurs at lower temperature when the structures get smaller[1].

2.2 Ultra high vacuum (UHV)

To ensure that the samples have clean surfaces before and during experiments, an ultra high vacuum is required. This vacuum also minimizes scattering from the gas phase. For electron surface spectroscopy it is necessary that the mean free path of the particles ($\sim 10^4$ m in UHV conditions) is much greater than the dimension of the apparatus (~ 1 m).

The SI unit describing pressure is the pascal (Pa), however this unit is not commonly used. The most common unit is torr, where 1 torr is defined as 1/760 atm. 1 torr is also equal to 1.333 mbar. High vacuum is classified as $10^{-6} - 10^{-8}$ torr, while ultra high vacuum is less than 10^{-9} torr. The vacuum pumps are cooled with a water circulation system. This is used to avoid heat expansion leading to wear or lubrication heating leading to failure.

A good ultra high vacuum is in the 10^{-11} torr range, but there are still gases present in the chamber. These gases should be hydrogen gas, water vapor, carbon monoxide and carbon dioxide. If significant ammount of oxygen or nitrogen (compared to the other present gases) are present in the vacuum chamber it can be an indication of a leak. Table 2.1 gives the m/z ratio of these gases. This can be measured with a mass spectrometer (see section 2.5), and is a good way to check for leaks in the chamber.

Turbomolecular pump ("turbo") A turbomolecular pump consists of stationary stator blades, and rotor blades spinning at very high speed (Typically in the 50,000 rpm range). When a gas particle from the chamber enters the pump it collides with a rotor blade, and its momentum is changed toward the outlet of the pump. Several such collisions in succession causes the particle to reach the outlet of the turbo pump [5]. The turbopump requires a low pressure pump to pump away the particles from the exhaust.

Ion pump An ion pump consists of a stainless steel anode and a titatium cathode. An electric field between the electrodes ionizes the gas between them and accelerates the ionized gas towards the cathode with enough energy to bury it deep in the metal [6]. Ion pumps work between 10^{-2} and 10^{-11} Torr, but has severly reduced lifetime when used above 10^{-5} Torr.

2.3 X-ray Photoelectron Spectroscopy (XPS)

This section is based on Brundle *et al.*[7] unless otherwise specified.

XPS is a surface sensitive spectroscopy technique in which soft x-rays impinges on a material and ejects photoelectrons. Electrons originating from the core levels of the material identifies the elements from the electron binding energy (BE). Additional information can be provided by small changes in the BE due to the binding of the electrons. Some of the ejected electrons move to the analyzer, where the kinetic energy (KE) of the electrons can be measured. The photon injection to electron ejection process happens on the order of 10^{-15} s, resulting in each electron giving a "snapshot" of the material at the time of impact.

2.3.1 Electron shell model

The electrons in an atom form shells around the nuclei with n^2 energy states in each shell, where $n = 1, 2, 3...$ is the nth shell from the core. However since electrons are fermions they obey the Pauli exclusion principle, and only 2 electrons (one with spin up and one with spin down, quantum number $s = \pm\frac{1}{2}$) can occupy each energy state. Thus there are $2n^2$ allowed energy states per shell. Each shell contain orbitals denoted $s, p, d, f, g...$ corresponding to the quantum number $l = 0, \pm1, \pm2, \pm3, \pm4...$, with $l \leq n - 1$. These orbitals can contain $2(2l + 1)$ electrons each, and fill in an order which minimizes energy. This order is $1s, 2s, 2p, 3s, 3p, 4s, 3d, 4p, 5s, 4d, 5p, 6s, 4f, 5d, 6p, 7s, 5f, 6d, 7p$ where the number denotes the n-value, and the letter is the l-value. One usually write the amount of electrons in each orbital as a superscript on the letter, as in $1s^2 2s^2 2p^4$ which would be oxygen. There is also a quantum number $j = l + s$ which is the spin-orbital coupling. This is written as a subscript to the letter, as in $4f_{7/2}$ and $4f_{5/2}$ or just $4f_7$ and $4f_5$ for short notation. This coupling can not occur for $l = 0 = s$.

2.3.2 Basic principles

The binding energy of the electrons ejected from a material can be determined by:

$$BE = h\nu - (KE + \phi) \tag{2.1}$$

where $h\nu$ is the energy of the incident photon and ϕ is the work function of the spectrometer. $h\nu$ and ϕ is known and thus a measurement of KE gives the binding energy of the electron. For each KE one can count the amount

of electrons impinging on the analyzer, and in the end one gets a spectrum, for example the Al_2O_3 spectrum in figure 2.3. Every peak can be identified by looking at the binding energies of known elements subjected to the same radiation, which can be found in literature [8].

The main peaks are caused by elastic scattering, where one photon ejects one electron with the momentum being preserved. The electron then travels unhindered from the material to the analyzer. The background radiation is caused by inelastic scattering, where the photon do not transfer all of its momentum to the electron, or by the photon ejecting an electron deeper into the material. This electron is then slowed down from the coloumb interaction with the atoms it encounters on the way out of the material, or it can cause secondary electrons to be ejected. All the electrons not from the elastic scattering will have lower KE, and will form a continous background spectrum at higher binding energy than its corresponding shell. According to (2.1) this reduced KE will be interpreted by the analyzer as an electron having higher BE.

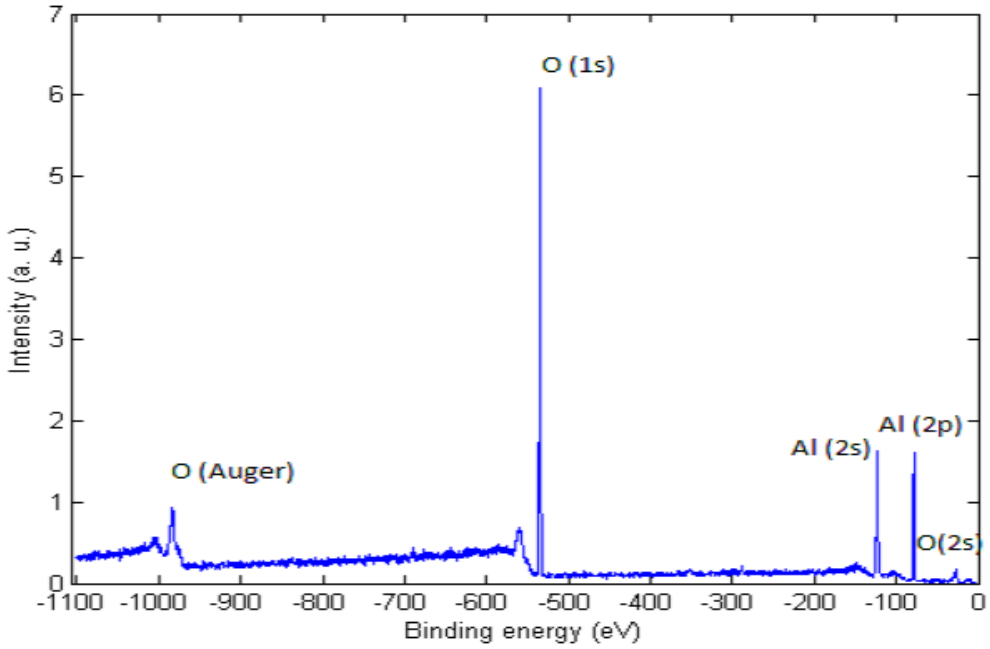

Figure 2.3: XPS spectrum for clean Al_2O_3. The different peaks are indentified. The minus sign on the binding energies is just a manipulation in matlab to display the spectrum in the right orientation.

When a photon ejects a core level electron, an electron from a higher energy level will jump down to the empty state. The surplus energy of this

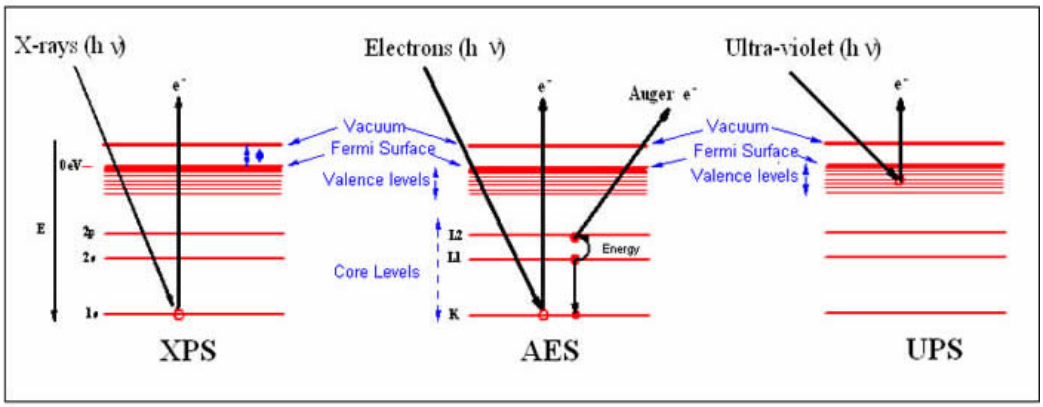

Figure 2.4: Schematic view of the photoelectron emission process. XPS is used to measure ejected core electrons (from a filled shell). AES (Auger spectroscopy) is used to measure secondary ejected electrons when a higher energy electron takes the place of an ejected core electron. UPS stands for ultraviolet spectroscopy and is used to measure electrons from the valence levels [9].

electron can either be ejected as a photon, or it can be used to eject a more loosely bound electron in the same atom. This is called an Auger electron and its energy is not dependent on the energy of the incident photon, only on the different energy levels within the atom. These electrons will also be observed in the XPS spectrum. See figure 2.4 for a schematic view of the different photoelectron processes.

The cross section for the photoionization, which is a measure of how probable it is that an incident photon ejects an electron, changes from orbital to orbital, from element to element, and different spin-orbital coupling. This causes different orbitals to display different sized peaks. Calculating the area of the peak and dividing it by its sensitivity factor (which is a measure of the cross section) gives the intensity of the peak. This can be used to calculate the thickness of a film on a substrate, as in (2.7). In the case of the surface not being a film, but clusters of atoms, (2.7) can also be used to calculate the thickness of a theoretical film, formed by all the surface atoms if they were redistributed in monolayers covering the entire substrate. This oversimplification described by (2.7) has many sources of error, but can be used to give an indication of the amount of material on a substrate.

Spin-orbit splitting is caused when the spin of the unpaired electron left behind in the orbital where an electron has been ejected is coupled with the angular momentum of that orbital. This can be seen as the splitting of a

single peak into two parts.

2.3.3 Instrumentation

Figure 2.5 shows a schematic view of an XPS spectrometer. The x-ray source is an Al-coated anode struck with electrons from a high voltage source. This causes Al K_α radiation of 1486.6 eV. This beam then impinges on a Si monochromator which focuses only the photons with energy 1486.6 ± 0.5 eV onto the sample. This improves the area onto which the x-ray beam hits, and also improves the linewidth of the system which gives a better resolution, but severely reduces the amount of photons that can impinge on the sample.

The electrons removed from the sample will lead to a charge up of insulating materials, which will affect the measurement greatly.

The lenses before the analyzer slow the electrons down, so they match the pass energy (PE) of the analyzer. The analyzer consists of two concentric hemispheres with a voltage between them. The voltage of the lenses and the analyzer allows only electrons of a certain energy to pass through the analyser to the detector, and by varying these voltages one is able to detect the entire spectrum of energies $KE < h\nu$. Only the voltages of the lenses are changed, with the analyzer voltage being kept at the pass energy. This ensures an absolute resolution across all electron energies. A lower pass energy gives a better resolution, but reduces the intensity. High energy electrons can damage the detector, so only $BE < 1100$ eV is normally used, unless higher BE is needed for the specific experiment. Computer software control all the aspects of the detection and analysis. To prevent heat build-up in the system, a liquid cooling system is used to transport heat away from the x-ray source.

2.4 Evaporation

A very common way of depositing a thin film is to heat the material until evaporation and let the evaporated material deposit on the substrate. In the case of metals, this can be done by running a current through a filament made from pure metal to heat it. Doing this evaporation in a UHV, means that the mean free path of the evaporated molecules are longer than the distance from the evaporator to the substrate, and the molecules travel directly from the evaporator to the substrate. By controlling the current (heat) and the exposure time, one can change the amount of deposited material. However the amount of deposited material may change from time to time. This can be caused by changes in the thickness of the metal leading to a change in

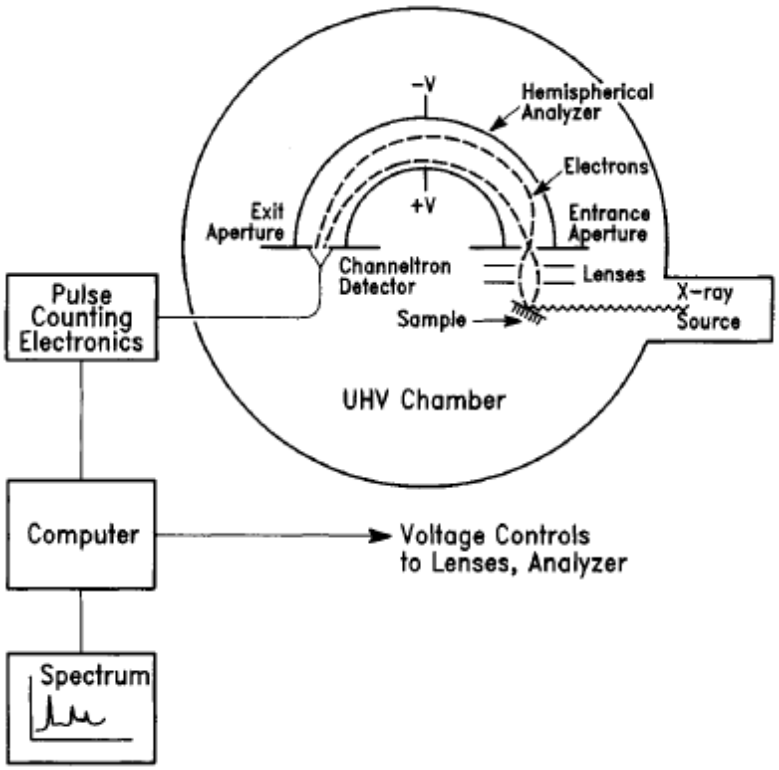

Figure 2.5: Schematic view of a hemispherical analyzer used in XPS experiments [7]. The x-rays hit the sample and electrons are relased. The electrons then travel to the lenses which slows them down to the pass energy of the analyzer. The electrons are detected and displayed on the computer.

resistance and thus a change in temperature.

One can estimate the thickness of the deposited layer by using XPS. This is done by measuring the spectrum of the substrate in an area where it has high intensity peaks, and by measuring the thin film spectra in an area where it has high intensity peaks. Figure 2.6 show a schematic view of a thin film on a substrate. Calculating the total area of the peak, and dividing it by the sensitivity factor and number of sweeps gives the intensity of that peak.

$$I = \frac{A}{SF \cdot n \cdot s} \tag{2.2}$$

where I is the intensity, A is the area of the peak, SF is the sensitivity factor, n is the number of iterations and s is the relative amount of electrons in the spin-orbital splitting if one only calculates for one peak in a split peak.

Using (2.2) the thickness of a film can be found using:

$$I_{sub} = \int_a^\infty e^{-\frac{x}{\lambda}} dx = \lambda e^{-\frac{a}{\lambda}} \tag{2.3}$$

$$I_{film} = \int_0^a e^{-\frac{x}{\lambda}} dx = \lambda(1 - e^{-\frac{a}{\lambda}}) \tag{2.4}$$

$$\frac{I_{film}}{I_{sub}} = \frac{\lambda(1 - e^{-\frac{a}{\lambda}})}{\lambda e^{-\frac{a}{\lambda}}} = e^{\frac{a}{\lambda}} - 1 \tag{2.5}$$

$$e^{\frac{a}{\lambda}} = \frac{I_{film}}{I_{sub}} + 1 \tag{2.6}$$

$$a = \lambda \cdot ln(\frac{I_{film}}{I_{sub}} + 1) \tag{2.7}$$

where I_{sub} and I_{film} is the intensity for the substrate and film, a is the thickness of the film, and λ is the electron mean free path.

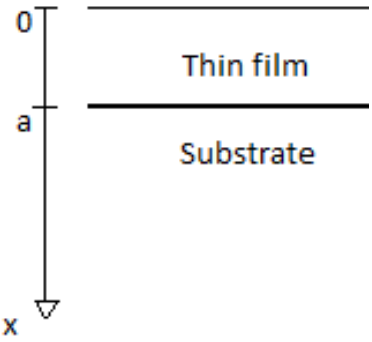

Figure 2.6: Schematic view of film on substrate

2.4.1 Diffusion Limited Aggregation (DLA) with active edge diffusion

In diffusion limited aggregation, particles move across a substrate with brownian motion (random walk) until it reaches a point where it is energetically favorable to adhere to the substrate. For a weakly interacting substrate it is less likely that the particle will adhere to just any random place on the substrate. The particle will move around until it reaches an imperfection on the substrate. This can be another particle that is allready adhered, or any imperfection in the lattice [10].

Fractal-island growth is related to the effect that a small tip on an island tends to become longer due to incomming adatoms prefering to stick to that tip. In DLA this effect is active throughout the process, but in real growth there is active edge diffusion since tips are wider than one atom[11].

In the case of metal being evaporated onto HOPG in a ultra high vacuum with a relatively low flux, the metal atoms will adhere at a few random places and some imperfections. Subsequent atoms that impinges on the surface will then adhere to these seeds and larger structures will form. The shape of these structures is then dependant on the properties of the carbon, the properties of the metal, and the already established distribution of metal on the carbon.

2.5 Quadrupole mass spectrometer

A quadrupole mass spectrometer (QMS) consists of 4 metal rods as can be seen in figure 2.7. This is the most common mass analyzer, with a mass range limit of m/z[†] 500 up to 4000 for some instruments.

The gas to be measured in the QMS is ionized and electric fields across the rods of the analyzer is used to separate the ions by their m/z ratio. There is a RF voltage[‡] applied across the two pair of rods in the analyzer, and on this RF voltage there is superimposed a direct current (DC) voltage. As can be seen in figure 2.7 the voltage squeezes the positive ions in the horisontal direction for the first half of the RF cycle, and in the vertical direction for the second half of the RF cycle. The field continues to alternate as the ions travel through the mass analyzer, generating a three-dimensional wave. The higher the m/z value is, the less the ion is accelerated by the changing field, but they are however more affected by the DC voltage than the low m/z ions. By changing the RF and DC voltage one can generate both highpass and lowpass filters for the ions, and proper scanning of these voltages is used to collect a complete mass spectrum[12].

During a measurement, the values of the voltages tell the QMS what mass to charge ratio is being measured. The amount of each m/z particle that impinges on the detector results in a current in the QMS. The value of this current is displayed on a computer interface, and is proportional to the partial pressure of the particles in the chamber. Table 2.1 gives the m/z value of the most common gases found in a vacuum system. Fragmentation of molecules into smaller parts occur. Nitrogen gas has a m/z of 28 which

[†] m/z refers to the mass of the ion divided by the unit charge of the ion, where m is given in atomic units and z is given in unit charges.

[‡] Radiofrequency alternating voltage in the range of 3 kHz to 300 GHz.

is the same as carbon monoxide, but has a fragmentation peak at 14. So a peak at $m/z = 14$ would indicate nitrogen in the chamber.

Table 2.1: The m/z ratio of the most common gases in a vacuum chamber. A good vacuum is dominated by hydrogen gas, water vapor, carbon monoxide and carbon dioxide. High ammounts of nitrogen and oxygen is an indication that there may be a leak in the system. Fragmentation of the molecules occur, and some are shown at several m/z ratios. Nitrogen if found at both 28 and 14, but since carbon monoxide is also found at 28 and always present, a peak at $n/z = 14$ would be the indication of nitrogen gas.

Molecule	m/z
Hydrogen (H_2)	2
Helium (He)	4
Water vapor (H_2O)	18
Carbon monoxide (CO)	28
Nitrogen (N_2)	28 and 14
Oxygen (O_2)	32
Carbon dioxide (CO_2)	44

2.6 Coulomb potential

When a photon in XPS removes an electron from a material there will be a positive charge left on the surface. When one has small structures on the surface, there will be a restriction on the area over which the positive charge can spread. This area will look like a hemisphere on the surface when sufficiently small. If this structure is a metal on top of a non-metallic substrate, this positive charge is not compensated quickly enough to avoid a coulomb attraction between the structure and the ejected electron. This attraction will remove an amount of energy from the electron [13]:

$$\Delta V = \frac{e^2}{8\pi\epsilon_0 r} \tag{2.8}$$

where $e = 1.6 \cdot 10^{-19}$ C is the electron charge, $\epsilon_0 = 8.85 \cdot 10^{-12}$ F/m is the electric permittivity and r is the radius of the hemisphere. The smaller the hemisphere gets, the larger the energy loss becomes. For example $r = 1$ nm gives $\Delta V = 0.72$ eV. This energy loss is seen as a reduction in the KE of the electron and according to (2.1) this shows up in the measured spectrum as having a higher BE.

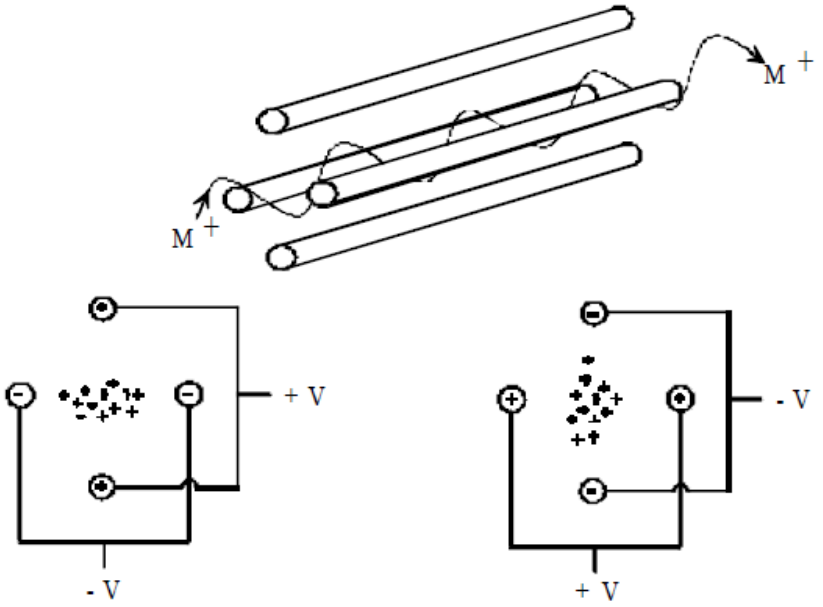

Figure 2.7: Quadrupole mass analyzer. The top image shows the ion trajectory through the quadrupole. The two bottom images show the ion focusing during the RF cycle. On the left is the first half and on the right is the second half of the cycle [12].

2.7 Scanning electron microscopy (SEM)

This section is based on Mills *et al.*[14] unless otherwise specified.

In scanning electron microscopy an electron source is used to supply a beam of electrons which is focused to a point on the sample. The point of focus (probe) is raster scanned over the sample, and electrons scattered from the surface are detected. Variation in the intensity of the detected electrons form the contrast of the image. The diameter of the probe basically defines the main resolution. It is dependant on the probe current, the energy of the primary beam, the size of the aperture and the working distance (the distance from the sample to the detector).

The electrons that strike the sample can collide either elastically (electron-nucleus) or inelastically (electron-electron). Figure 2.8 show the origin of the different signals within the sample. Elastic collisions produce backscattered electrons carrying mainly compositional data. Inelastic collisions deposits energy in the sample, which then relaxes back to the ground state by releasing secondary electrons, x-rays and heat phonons. These backscattered and secondary electrons are detected by different detectors, and an image of the sample can be produced.

The secondary electrons originates in the top few nanometers of the sample, and for this reason it is mainly used for topography information. The electrons can mainly be caused by interaction between the primary beam and the sample, or by interaction between backscattered electrons and the sample. Steep surfaces and edges tend to let more electrons escape, leading to brighter areas on the image. There are several types of secondary electron detectors, but the most common one is an in-lens type as it is known to produce better resolution.

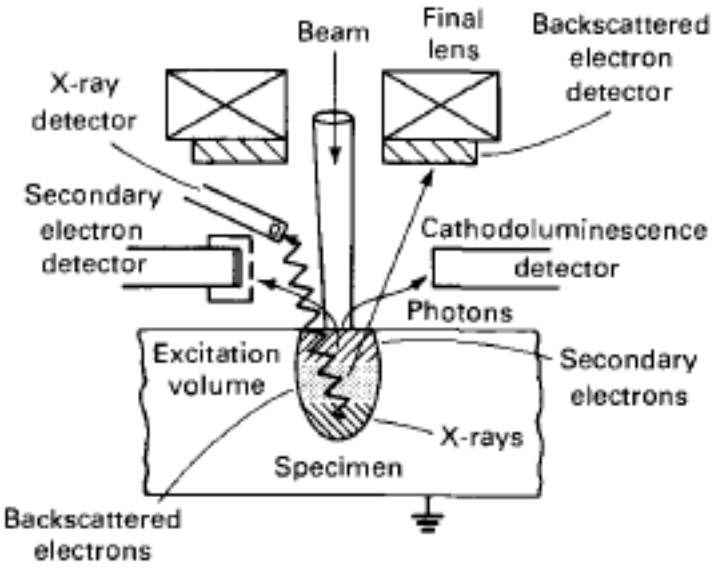

Figure 2.8: The origin of the different electrons within the excitation volume for SEM can be seen, as well as the detection system [14].

Chapter 3

Experimental

3.1 Experimental column

The experimental column consists of 4 major chambers: the loading dock, the preparation chamber with a sample storage area, the reaction chamber and the analysis chamber as can be seen in figure 3.1. All these chambers can be closed off from each other, and whenever an area is not in use it is closed off from the others to avoid problems with the vacuum if any faults were to happen in one part of the column.

Some times it is necessary to turn of the vacuum in the chamber and expose it to atmosphearic conditions. This is necessary whenever one wants to replace any of the parts of the chamber. When the vacuum pumps are turned back on, the chamber needs to be baked out for several days (up to 48 hours) to desorbe any gas sticking to the inside of the chamber. Before doing this bakeout it is recommended to do a check for leaks. For this check the QMS is turned on in the chamber, and helium gas is pumped around all the gaskets of the chamber on the outside. If the ammount of helium in the chamber rises, then there is a leak that needs to be fixed before baking.

Loading dock The loading dock is used to insert and extract samples from the column, and has its own small turbopump to supply the vacuum. It also houses the manipulator used to move the samples between the loading dock, storage area, preparation chamber and reaction chamber. To maintain a low pressure in the preparation chamber, the valve to the loading dock is not opened while the pressure is above 10^{-8} torr. When loading samples, the loading dock is exposed to atmosperic pressure for as little time as possible. Care is taken not to contaminate the parts on the inside of the chamber.

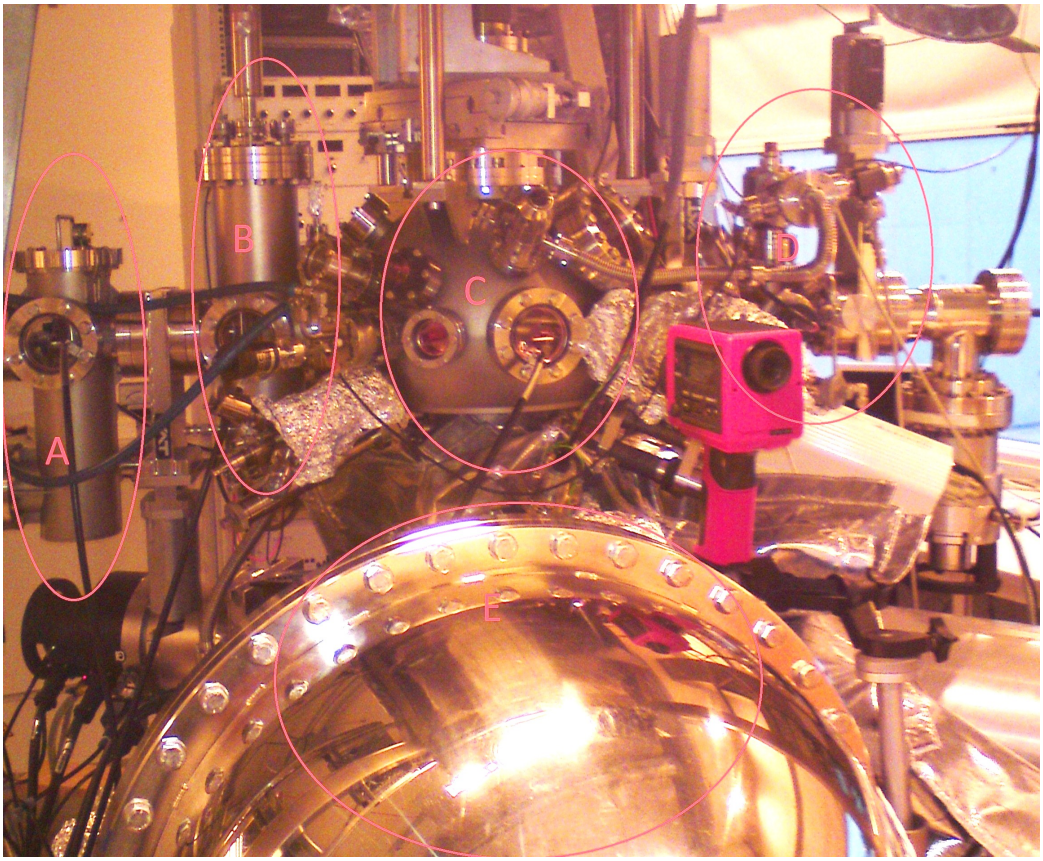

Figure 3.1: The experimental column. Part A is the loading dock, B is the sample storage area, C is the preparation chamber and D is the reaction chamber. The large metal hemisphere at E is the hemispehrical analyzer. Directly beneath the preparation chamber and behind the analyzer is the analysis chamber.

Preparation chamber The preparation chamber is where the sample is loaded onto the column manipulator from the loading manipulator. It also houses a storage area where up to 6 sample holders can be placed (to avoid removing them from the vaccum). Both the evaporator and the sputter sources are in this chamber. The pressure is maintained by a turbopump. The column manipulator can be moved vertically by a computer controller motor, and the rotation and pitch of the sample can be adjusted manually. The manipulator has electrical connections for the thermocouple and the filament in the sample holder. Degassing of the samples were performed in this chamber with all other chambers closed off.

Analysis chamber Below the preparation chamber is the chamber which houses the monochromatic Al K_α x-ray source (Scienta), the SES2002 analyzer (Scienta) and the electron gun. Its pressure is maintained by an ion pump and a turbopump. The analysis chamber turbopump exhaust into the same low vacuum pump as the turbopump in the preparation chamber. This leads to a small amount of pressure leak from the preparation chamber to the analysis chamber, and therefore the analysis turbopump is allways closed off when the analysis chamber is closed off from the preparation chamber. To maintain a ultra high vacuum in the analysis chamber, the valve between it and the preparation chamber is not opened unless the pressure in the preparation chamber is below 10^{-9} torr.

Reaction chamber The reaction chamber is connected to the preparation chamber, and houses electrical connections for heating the sample and measuring temperature. The chamber has a small turbopump to supply the vacuum, and also inlets for gases (including oxygen). Closing the chamber off from the preparation chamber and the small turbopump, one can work with atmospheric pressures of gases if needed. To maintain the pressure of the preparation chamber, the valve between the chambers is not opened unless the pressure is less than 10^{-8} torr in the reaction chamber.

Differentially pumped mass spectrometer The mass spectrometer (Pfeiffer vacuum - Prisma) can be seen in figure 3.1 just under reference D (the white triangular box). The QMS can measure any gas molecule that arrives at the analyzer through normal dispersion in the chamber. This can lead to reduced sensitivity when measuring the gases present at the surface of a sample.

Figure 3.2 shows the QMS moved to a new position. Here a turbo pump is connected to draw gas molecules through the QMS and thus increase the analyzers ability to detect molecules present at the tip of the nozzle. The presence of this dedicated turbo pump is why the system is called differentially pumped. This setup should increase the sensitivity of the QMS and also allow detection of gases that react at the surface of the sample or are desorbed from the sample.

3.2 Sample preparation

The samples used in the experiments were HOPG for all but one measurement which used a piece of pyrolytic graphite (sample 6). The HOPG samples were obtained from MaTeck and had physical dimensions of 12 mm by 12 mm by

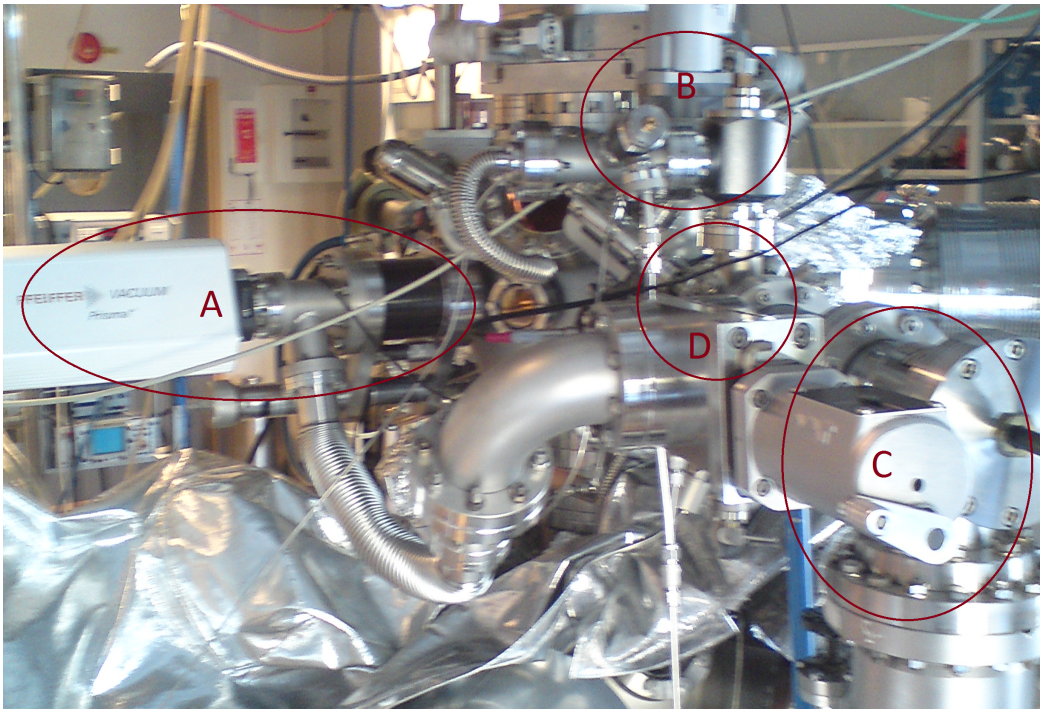

Figure 3.2: The experimental column after the rebuild to facilitate a differentially pumped mass spectrometer system. Part A is the quadropole mass spectrometer. Part B is a valve which needs to be closed to differentially pump the system. Part C is a valve (the part with a handle) and directly beneath it is the turbo pump used to pump the mass spectrometer system. Part D is the reaction chamber (part D of figure 3.1)

1 mm. The pyrolytic graphite sample was obtained from Goodfellow and was cut to size (approximately the same size as the HOPG samples, but only 0.2 mm thick) using a scalpel.

The samples needed to be affixed to holders designed to work in the UHV chamber. To avoid additional contamination on the samples and sample holders, gloves were worn at all times when working with any material destined for the vacuum chamber.

The sample holders are designed with grooves to fit with the tongues inside the vacuum chamber to keep the holder in place. They have one small and one larger lip which indicate the way they are to be inserted. The back of the holders, which can be seen in figure 3.3b, have 6 screws which doubles as electrical contacts. Two contacts is for passing current to the heating filament, two is for the different conductors for the thermocoupling, and the two last contacts are used for grounding the sample holder.

(a) (b)

Figure 3.3: (a) show the front of the sampleholder. The thermocouple wires pertrude at the bottom part of the holder. (b) show the connections on the back of the sample holders. As the holder is seen in (b) the top two connections are for the thermocouple, the middle two are for the heating filament and the bottom two are for grounding. In (b) the sample holder is rotated such that the top part is directly behind the lower part of (a)

Sample mounting The samples were mounted on a holder seen in figure 3.3a. The thermocouples were pressed under the sample and the mask was placed on top in order to keep the sample in place. This sample holder was heated by passing current through a filament inside the holder. Care was taken to avoid scratches on the sample surface. To obtain a new pure surface, a piece of scotch tape was used to remove the top layer of carbon from the sample. This method is the easiest way of obtaining a clean, smooth surface on HOPG.

Degassing Degassing had to be performed on all the samples to evaporate any gas adsorbed to the surface. This degassing was done using a PID controller* connected to the thermocouple and a power supply, which in turn was connected to the heating filament in the sample holder. The samples were heated repeatedly to 930 K until a UHV vacuum was maintained at the peak temperature.

Sputtering An ion source is used to turn a gas into a plasma. This plasma can then be accelerated by electrical fields. The plasma is directed toward the sample surface and moment (and energy) transfer from the plasma atoms ejects atoms from the sample. By using an inert gas, like argon, one avoid

*The controlling software was written by Steinar Thorshaug for his project work in 2004.

problems related to chemical bonding of the plasma with the surface, and also argon atoms are heavy enough that atoms on the sampe surface are easily ejected. The ejected atoms are then carried out of the vacuum chamber by the pumping system. The pressure in the chamber was increased to $6.5 \cdot 10^{-6}$ torr and the sample was rotated to face the sputter source at an 75° angle before starting the sputtering. All sputtering was performed at an ioncurrent of 18 mA.

Figure 3.4 show a contaminant protecting a small area of a sample surface from being sputtered. One can also see how the metal has been sputtered away from the surface in the gray areas.

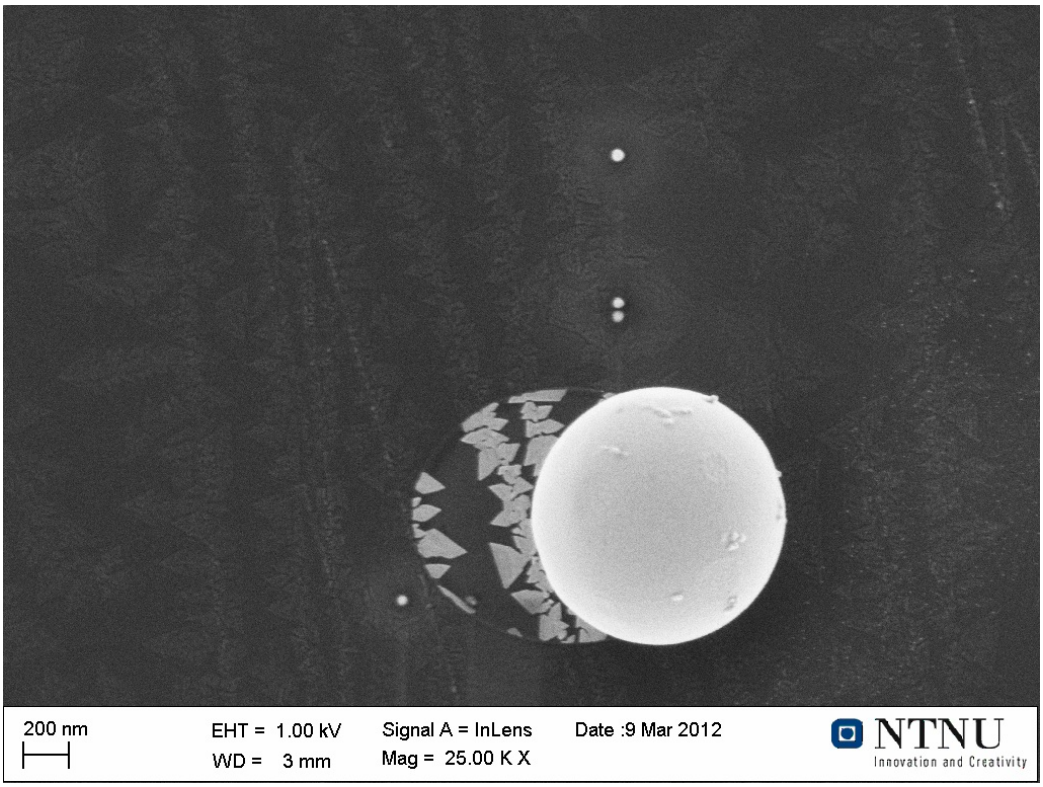

Figure 3.4: The round object seen on the image is some form of contaminant which has shielded parts of the metal on the surface from being sputtered. The white areas to the left of the ball is gold and the black background is graphite. The gray areas had gold on it before the sputtering. The scale can be found in the bottom left of the image.

Evaporation To deposit platinum onto the samples, a simple evaporator is used. It contains a coiled Pt-wire (filament) through which a current flows.

This current heats the filament and atoms are evaporated away. The atoms distribute, and deposit, throughout the chamber, including the sample. For gold evaporation a similar setup to that of platinum was used. However instead of running a current directly through a gold wire, a current was run through a tungsten wire basket shaped coil which had a nugget of gold in its centre. This indirect heating of the gold could lead to small differences in evaporation flux over time.

To have similar conditions for each sample before deposition, the samples were heated to 810 K and let cool down to 310 K and kept at that temperature during the evaporation, except for samples 11,12 and 13 which were cooled down to 150 K, 200 K and 250 K respectively. The samples were rotated to directly face the filament before evaporation. The evaporation source was cooled with water. Following the evaporation of samples 15 and 16, the platinum wire in the evaporator broke off and had to be replaced.

3.3 Measurement

Following cleaning procedures, the samples were deposited with Au or Pt according to table 3.1. The pressure in the preparation chamber was allowed to drop to acceptable levels ($< 10^{-9}$ torr) before opening the valve to the analysis chamber and moving the sample down.

For XPS, an acceleration voltage of 13 kV was always used, and the filament current was increased high enough to ensure a 19.1 mA discharge current. This meant a filament current of about 13.86 A. Ensuring that the discharge current was always the same meant that the intensity for different measurements could be compared directly. The temperature in the x-ray chamber was kept at 55 °C with a heat source.

Following the evaporation, a XPS sweep was performed to make sure no contaminants were added with the evaporation process.

After evaporation, some of the samples were sputtered for some intervals to look at the change (if any) in the BE and changes in the nanostructures. Table 3.2 give the times at which the XPS data was recorded during the sputter process. Before starting sputtering, the sample was rotated and moved to face the ion beam.

After evaporation, and after each round of subsequent sputtering, a XPS spectra of the main peak of carbon ($1s$) and gold ($4f$) or platinum ($4f$) was recorded. Table 3.3 give the settings used for measuring each spectra.

Figure 3.5 shows the peak for Au_4f right after evaporation on sample 4. The shape of the peaks looked similar to this for all XPS measurements of Au_4f for the different samples . Figure 3.7 shows the peak for C_1s

right after evaporation on sample 4. All XPS measurements of the C_1s had the same shape for all samples. Figure 3.6 shows peak for Pt_4f right after evaporation on sample 20. The shape of the peaks looked similar for alle XPS measurements of the Pt_4f on the different samples, however a small change in the positions of the peak were observed. MATLAB was then used to calculate the area under the peaks. (2.2), with data from table 3.4, could then be used to calculate the intensity of the peak. This was done for the peak for both carbon and metal following each round of sputtering or evaporation. (2.7) could then be used to get an estimate for the thickness of the metal on the graphite.

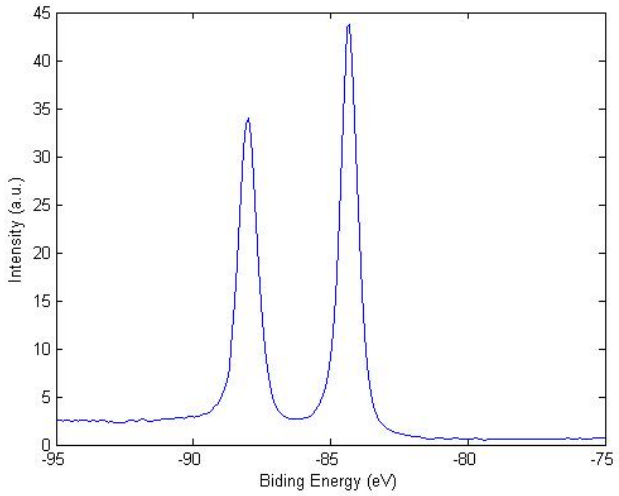

Figure 3.5: Au_4f peak from sample 4 right after evaporation. The peak is used to calculate the intensity of gold.

A reactivity study was conducted on samples 18-21 after platinum evaporation, aswell as before evaporation on sample 20 for a baseline. The mass spectrometer was placed so that the tip of the probe was positioned directly in front of the sample just a few millimeter from the surface. The valves in figure 3.2 were positioned so that the QMS was differentially pumped.

The current value of the m/z ratio of oxygen, carbon monoxide and carbon dioxide was recorded as a function of time. Oxygen was then introduced into the chamber until the current value was approximately $5 \cdot 10^{-7}$ A, and carbon monoxide was also introduced until the current value was approximately the same as oxygen. After about 1 min the pressure of oxygen was incresed until about the double of carbon monoxide, and 1 min after this the oxygen pressure was reduced to about half that of carbon monoxide. To allow direct comparison of the measured pressures of the different samples, the

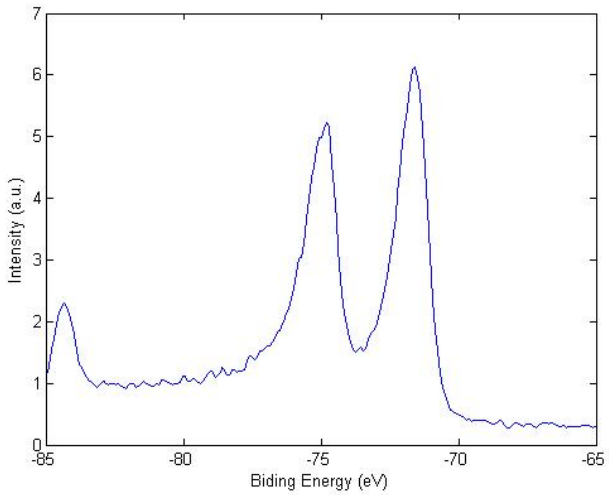

Figure 3.6: Pt_4f peak from sample 20 right after evaporation. The peak is used to calculate the intensity of platinum. Note the small peak on the left side of the spectrum which is discussed later.

current value of carbon dioxide was devided by the current value of carbon monoxide. Any change in the oxidaztion of carbon monoxide would show up as changes in these spectrums.

Figure 3.8 shows how the current value of CO_2 (or more precisely a m/z value of 44) as a function of time.

Following the sputtering and subsequent XPS analysis, the samples were removed from the vaccum chamber and taken to be imaged with a (field emission) Zeiss Ultra SEM. This was done to find out how the metal on the surface looked.

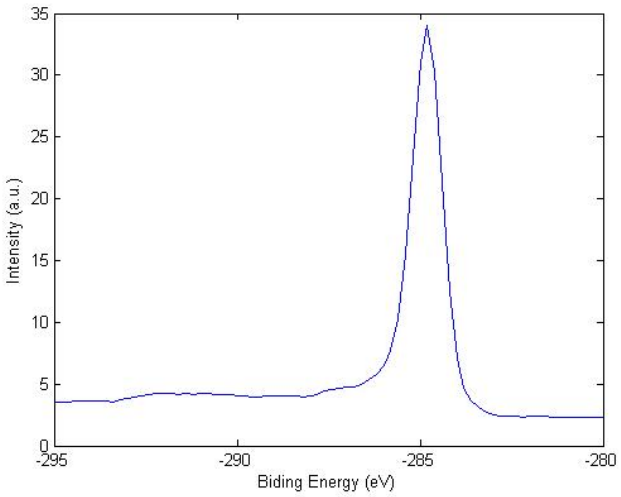

Figure 3.7: C_1s peak from sample 4 right after evaporation. The peak is used to calculate the intensity of carbon.

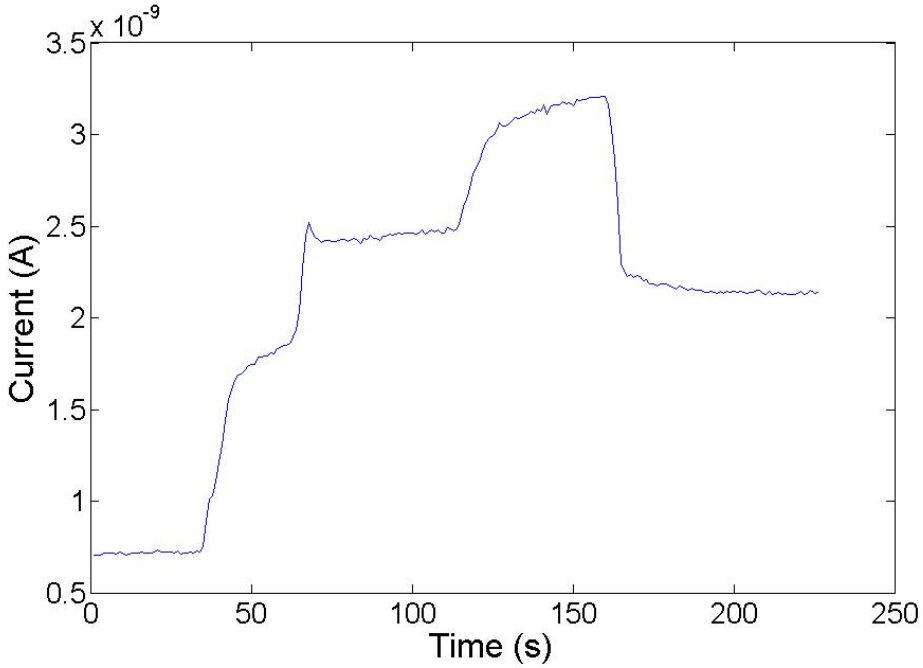

Figure 3.8: QMS measurement of CO_2 as a function of time. The QMS current measured for $m/z = 44$ as a function of time for a reactivity study.

Table 3.1: The amount of metal evaporated onto the different samples. All samples were HOPG except sample 6, which was the pyrolytic graphite foil. Sample 14 is missing because it was accidentally destroyed before being imaged with SEM. Intensity ratio is calculated using XPS data as intensity of metal devided by intensity of substrate.

Sample	Metal	Temperature (K)	Current (A)	Evaporation time (min)	Intensity ratio
1	Au	310	10	20	0.351668
2	Au	310	10	8	0.123576
3	Au	310	9.5 then 9.75	15 then 10	0.178215
4	Au	310	9.75	10	0.108992
5	Au	310	9.75	10	0.184183
6	Au	310	9.75	10	0.232604
7	Au	310	9.75	10	0.389297
8	Au	310	9.5	2	0.072582
9	Au	310	9.5	3	0.095825
10	Au	310	9.5	1	0.036457
11	Au	150	9.5	2	0.088693
12	Au	200	9.5	2	0.105470
13	Au	250	9.5	2	0.087052
15	Pt	310	9.5	10	0.024001
16	Pt	310	9.5	20	0.045788
17	Pt	310	9.5	20	0.039372
18	Pt	310	9.5	3	0.003293
19	Pt	310	9.5	6	0.006344
20	Pt	310	9.5	12	0.011361
21	Pt	310	9.5	24	0.025727
22	Au	310	9	0:15	0.009891
23	Au	310	9	0:30	0.023201

Table 3.2: The total amount of sputtering performed on samples after evaporation, and after which time each sputtering was stopped. The samples that are not in this table were not sputtered. Samples 3 and 7 were removed from the vacuum and imaged with SEM before being reintroduced to the vacuum for sputtering. The other samples were not removed from vacuum until all sputtering was done.

Sample	Total sputter time (min)	Sputter intervals (min)
2	84	7, 15, 30, 45, 60, 72, 84
3	9	9
4	10	10
5	15	15
7	9	9
17	4:30	4:30

Table 3.3: The regions being surveyed during XPS measurements for the various materials.

Name	BE range (eV)	Number of iterations	Pass energy (eV)
sweep	$0 - 1100$	1	500
C_1s	$280 - 295$	5	500
Au_4f	$75 - 95$	10	200
Pt_4f	$65 - 85$	10	200

Table 3.4: The sensitivity factors used in (2.2) *to calculate the intensity and subsequent thickness for the measurements.*

Peak	Sensitivity factor
C_1s	1
Au_4f	17.66
Pt_4f	15.97

Chapter 4

Results

4.1 Gold deposited on HOPG

Figure 4.1 shows gold nanostructures on sample 3 following 15 min evaporation at 9.5 A and 10 min evaporation at 9.75 A, corresponding to an intensity ratio of $Int_{Au}/Int_C = 0.1782$. There are dendritic structures and spaghetti-like structures. In figure 4.2 the same sample has been sputtered for 9 min. The same type of structures are still present, but the areas have been partly removed leading to small gold dots instead of a continuous layer of gold. The amount of gold has been reduced to an intensity ratio of $Int_{Au}/Int_C = 0.1212$. The "spine" of the spaghetti-like structures still have a bright white colour, indicating that the thickness of the gold is not greatly changed by the sputtering.

Figure 4.3 shows gold spaghetti-like nanostructures on sample 22 following 15 s evaporation at 9 A, corresponding to a intensity ratio of $Int_{Au}/Int_C = 0.009891$.

In figure 4.4 one can see gold nanostructures from sample 23 following 30 s evaporation at 9 A, corresponding to a intensity ratio of $Int_{Au}/Int_C = 0.02320$. Spaghetti-like structures with a small amount of branching can be seen, aswell as some small gold triangles.

The structures on sample 10 in figure 4.5 are formed after 1 min evaporation at 9.5 A, corresponding to an intensity ratio of $Int_{Au}/Int_C = 0.03646$. In addition to spaghetti-like structures with small branching, many smaller gold islands with various shapes can be seen.

Figure 4.6 shows gold nanostructures on sample 8 following 2 min of evaporation at 9.5 A, equivalent to an intensity ratio of $Int_{Au}/Int_C = 0.07258$. Branched spaghetti-like structures are present, as well as smaller structures comprised of multiple triangles.

Figure 4.1: Gold nano-dendrite on HOPG. This SEM image from sample 3 shows the dendritic and spaghetti-like nanostructures of gold evaporated onto graphite at 310 K *for 25 minutes. The scale can be found in the bottom left of the image.*

Sample 9 was evaporated for 3 min at 9.5 A, with a corresponding intensity ratio of $Int_{Au}/Int_C = 0.09582$. Figure 4.7 shows the gold nanostructures on the surface. Spaghetti-like structures with triangular branching can be seen. More complex dendritic structures consisting of triangular branches which also have additional branches with triangular structures.

Figure 4.8 shows the structures on the surface of sample 7. Gold was evaporated for 10 min at 9.75 A on this sample. The intensity ratio was $Int_{Au}/Int_C = 0.3893$. Spaghetti-like structures can be seen, as well as nanoislands that are not connected to other particles. The amount of branching is significant on both the spaghetti and the islands, with the previously seen triangular shapes still present. The different intensity of the white areas (gold) indicate a difference in thickness of the nanostructures. There also seem to be boundries between the different structures, indicating that they do not connect with eachother. This sample was sputtered for

9 min and figure 4.9 shows the effect of sputtering. The intensity ratio was $Int_{Au}/Int_C = 0.01110$. The same gold dots as in figure 4.2 can be seen. Parts of the structures are not reduced to dots since the thickness of the nanostructures varies.

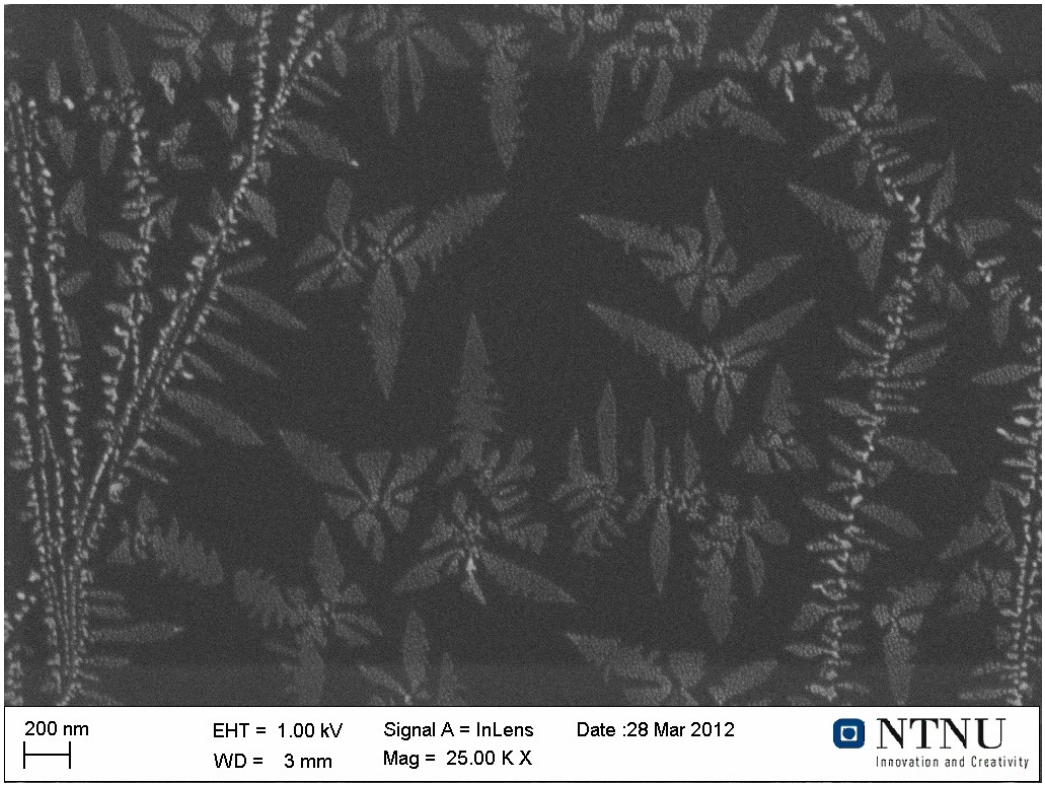

Figure 4.2: The effect of sputtering on gold nano-dendrites. This SEM image shows gold nano-dendrites and spaghetti-like structures on sample 3 after having been sputtered for 9 minutes. The bright white color on the "spine" of the spaghetti indicate that the thickness of the gold is not significally changed by the sputtering. The scale can be found in the bottom left of the image.

Sample 6 was not a HOPG substrate, but a pyrolytic graphite foil that was cut to size. Figure 4.10 shows gold nanostructures evaporated for 10 min at 9.75 A, corresponding to an intensity ratio of $Int_{Au}/Int_C = 0.2326$. The familiar triangular shapes are also seen on this substrate, including branching into more triangular shapes. The spaghetti-like structures was also present on this substrate, allthough they are not that predominant in this image.

Samples 11 and 12 were cooled down to 150 K and 200 K, respectively, during evaporation. Figure 4.11 shows how the gold formed on the surface on sample 11. There are no clear nanostructures, just a random aggregation

of gold without any boundries or other shapes seen on the other samples. The same random structures can be seen on sample 12.

Figure 4.12 shows how gold formed on the surface of sample 13. There are no nice uniform structures like the ones found on the samples prepared at room temperature, but the formation of islands shows that diffusion across the surface has taken place. These structures are different from the ones found on sample 11 and 12 in that they do not form a continous connected pattern of gold.

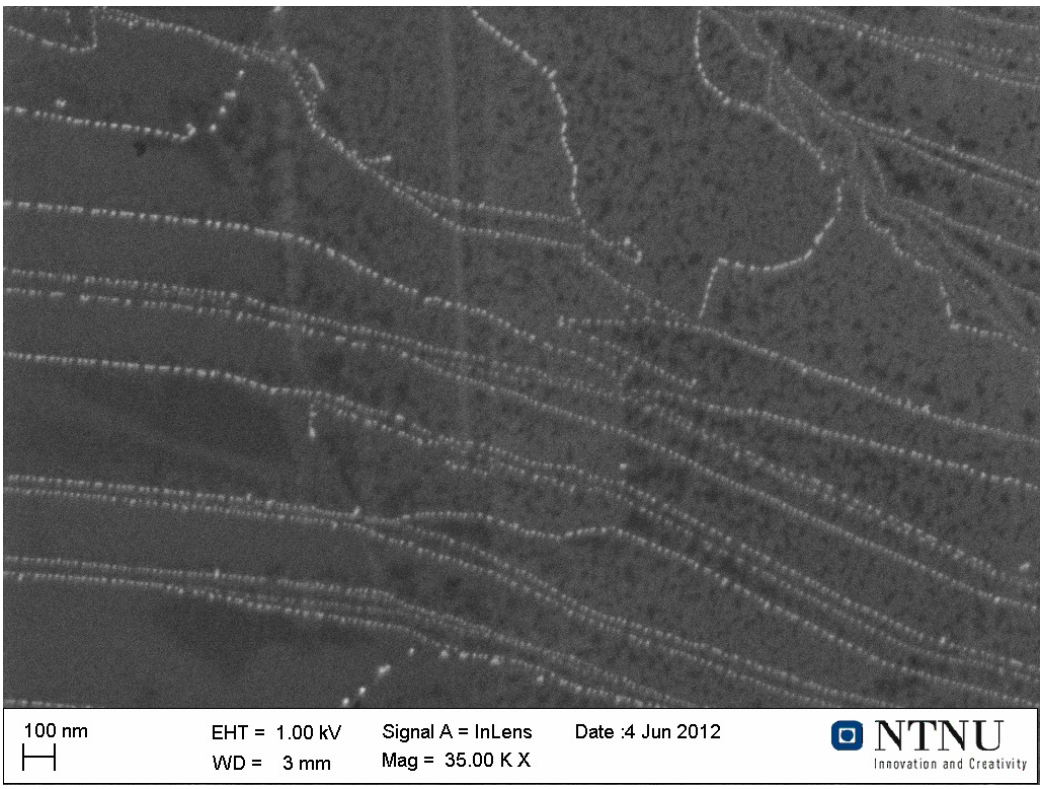

Figure 4.3: Gold nanostructures on HOPG. This SEM image from sample 22 shows nanostructures of gold evaporated onto graphite at 310 K *for 15 seconds. The gold has gathered in spaghetti-like structures. The scale can be seen in the bottom left of the image.*

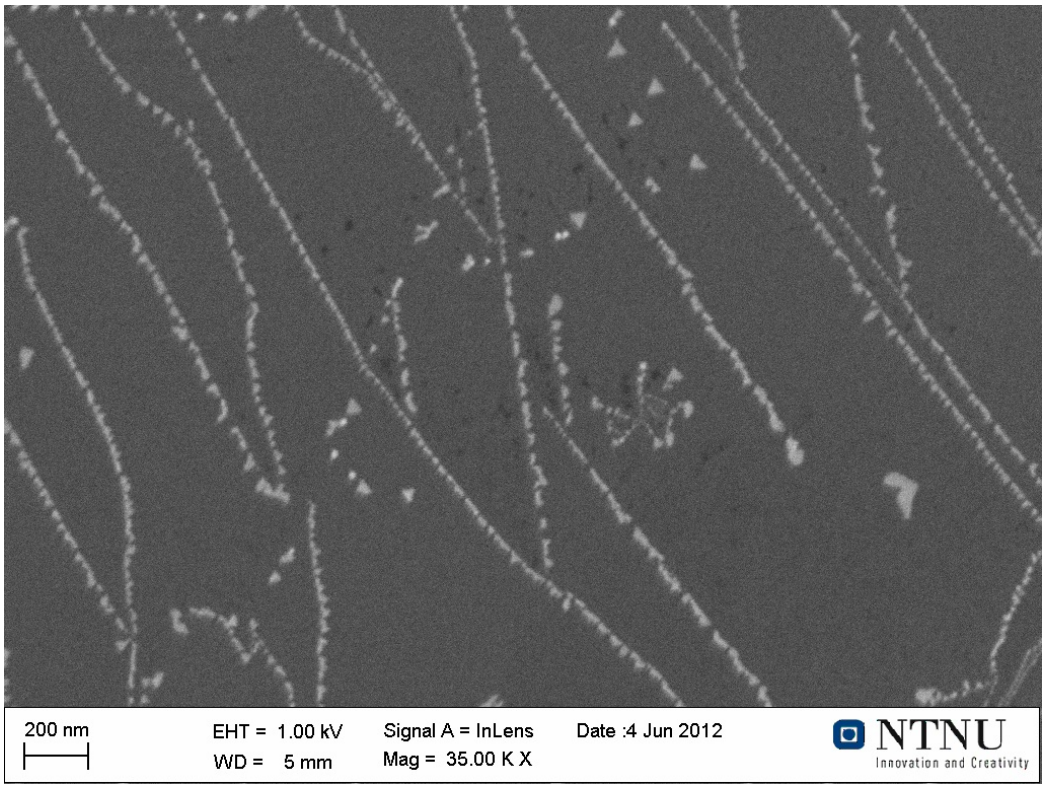

Figure 4.4: Gold nanostructures on HOPG. This SEM image from sample 23 shows nanostructures of gold evaporated onto graphite at 310 K *for 30 seconds. The spaghetti-like structures has functioned as seeds for small branches of gold. Small triangular gold nanoislands are also seen. The scale can be seen in the bottom left of the image.*

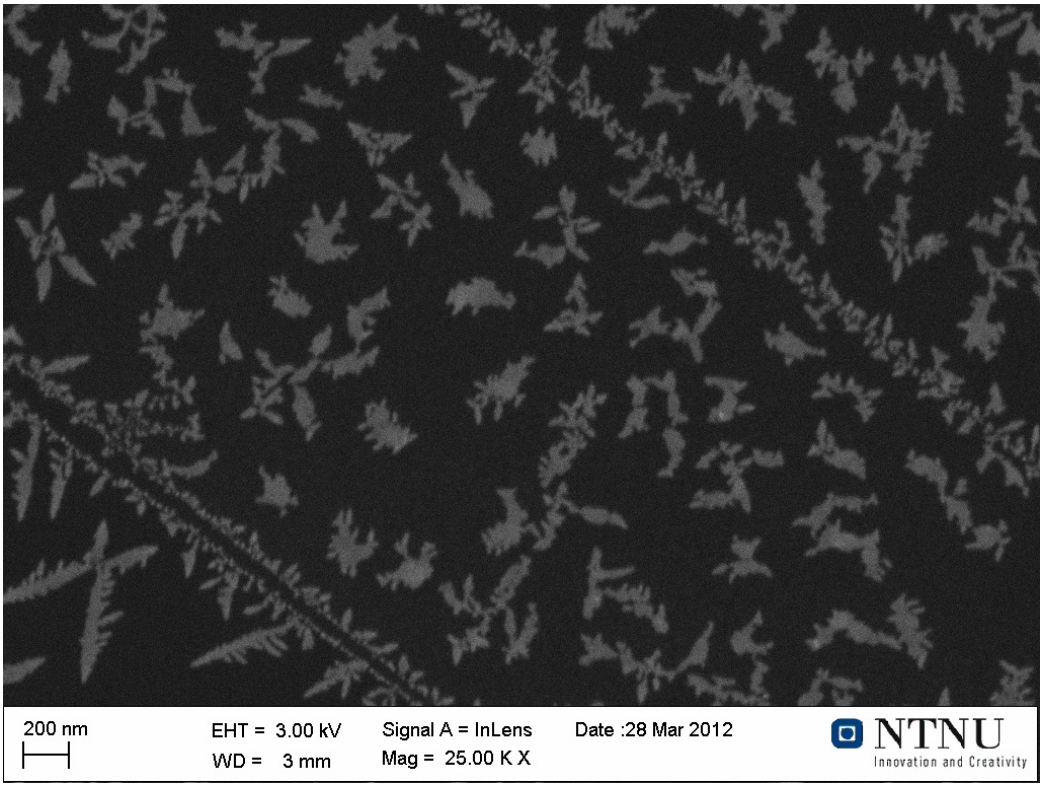

Figure 4.5: Gold nanostructures on HOPG. This SEM image from sample 10 shows nanostructures of gold evaporated onto graphite at 310 K *for 1 minute. The spaghetti-like structures acts as seeds for more complex branches. The gold nanoislands have a more random shape than seen in other images. The triangular structures are not readily seen. The scale can be seen in the bottom left of the image.*

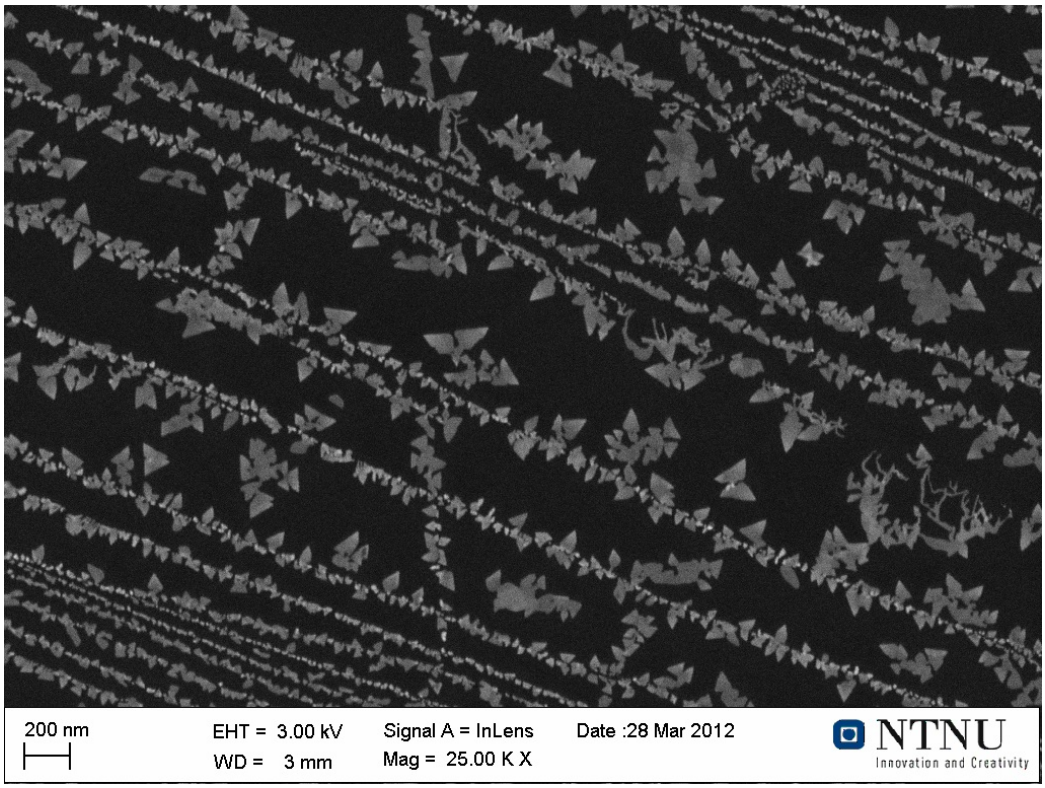

Figure 4.6: Gold nanostructures on HOPG at 2 minutes of evaporation. This SEM image from sample 8 shows nanostructures of gold evaporated onto graphite at 310 K *for 2 minutes. Spaghetti-like structures and nanoislands both have branching with a triangular shape. The scale can be seen in the bottom left of the image.*

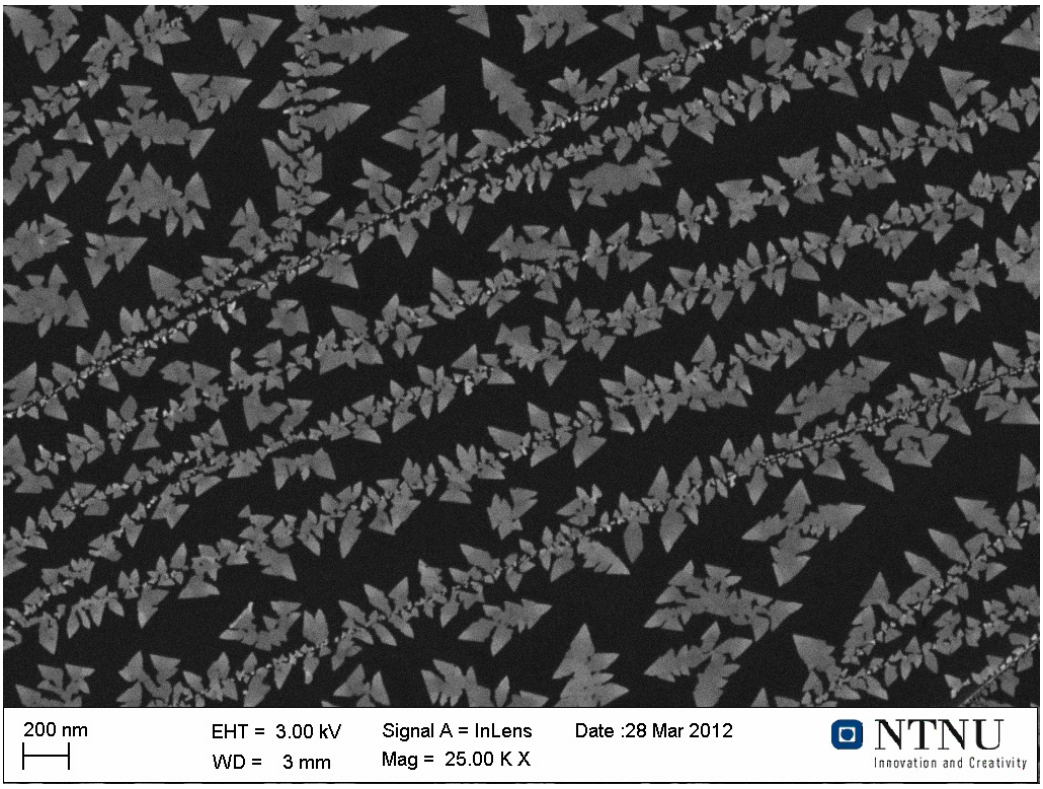

Figure 4.7: Gold nanostructures on HOPG at 3 minutes of evaporation. This SEM image from sample 9 shows nanostructures of gold evaporated onto graphite at 310 K *for 3 minutes. The spaghetti-like structures and nanoislands both have complex branching, which all have a triangular shape. The scale can be seen in the bottom left of the image.*

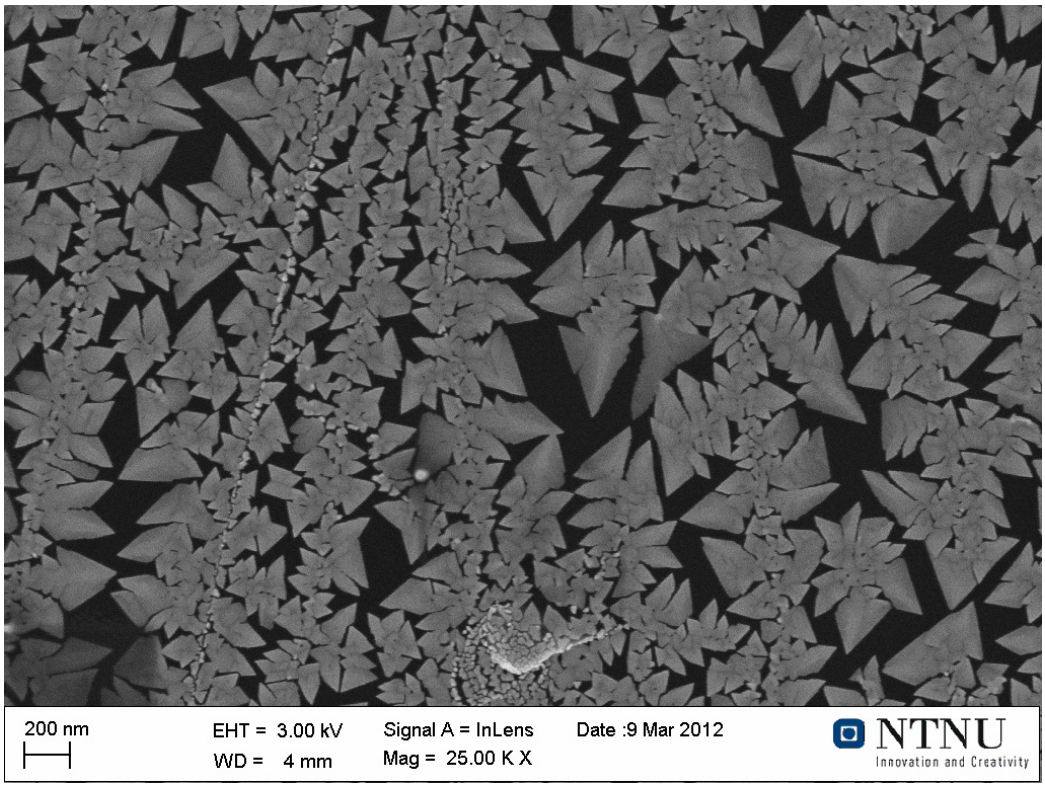

Figure 4.8: Gold nanostructures on HOPG at 10 minutes of evaporation. This SEM image from sample 7 shows nanostructures of gold evaporated onto graphite at 310 K *for 10 minutes The spaghetti-like structures and nanoislands have complex branching, which all have a triangular shape. The different intensity of the white pixels in the image (the gold) indicate that the gold layer is thicker towards the center of the structures than at the boundries. The scale can be seen in the bottom left of the image.*

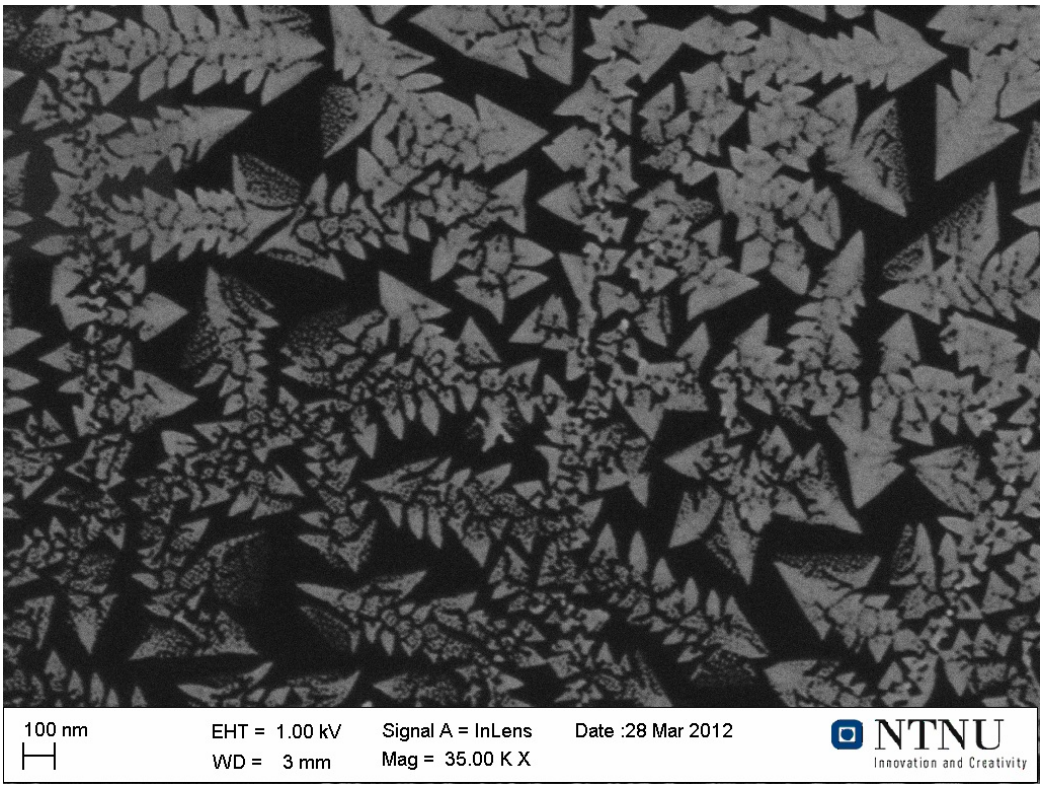

Figure 4.9: Gold nanostructures on HOPG at 10 minutes of evaporation and 9 minutes of sputtering. This SEM image shows the nano-dendrites on sample 7 after 9 minutes of sputtering. In some areas the gold has been mostly removed and what remains are gold dots, still in the shape of the dendrites. The scale can be seen in the bottom left of the image.

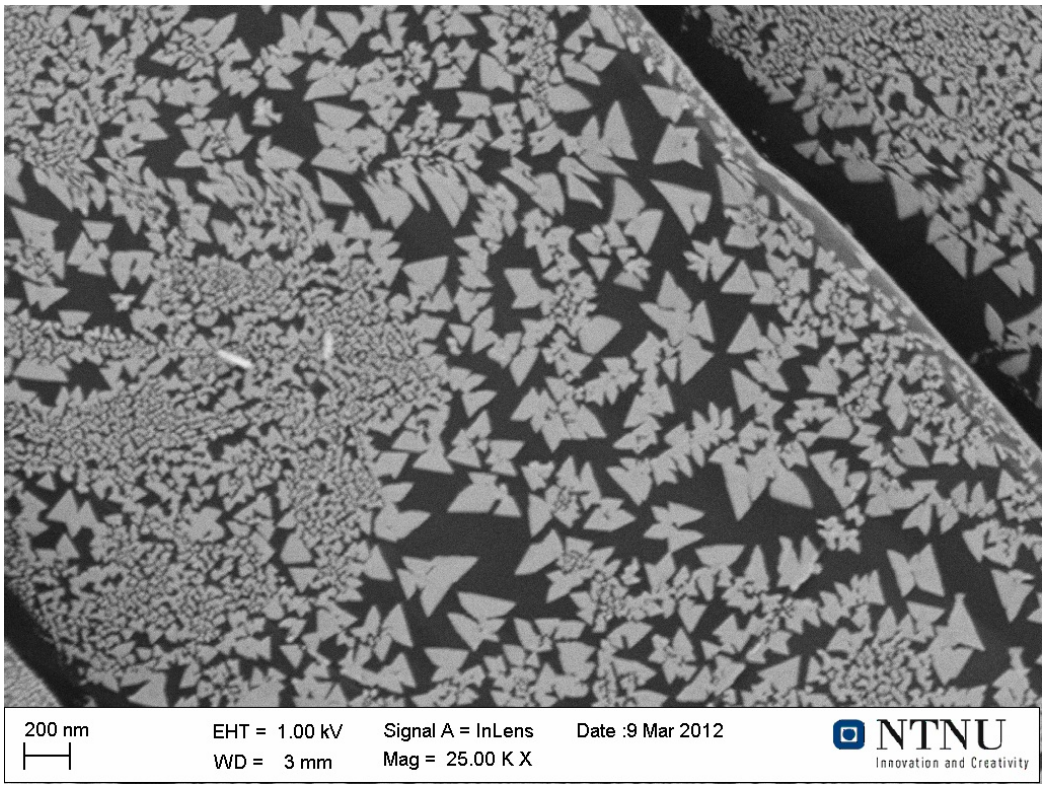

Figure 4.10: Gold nanostructures on pyrolytic carbon foil at 10 minutes of evaporation. This SEM image from sample 8 shows nanostructures of gold evaporated onto graphite foil at 310 K *for 10 minutes. Gold nano-dendrites with triangular branching can be seen. The scale can be seen in the bottom left of the image.*

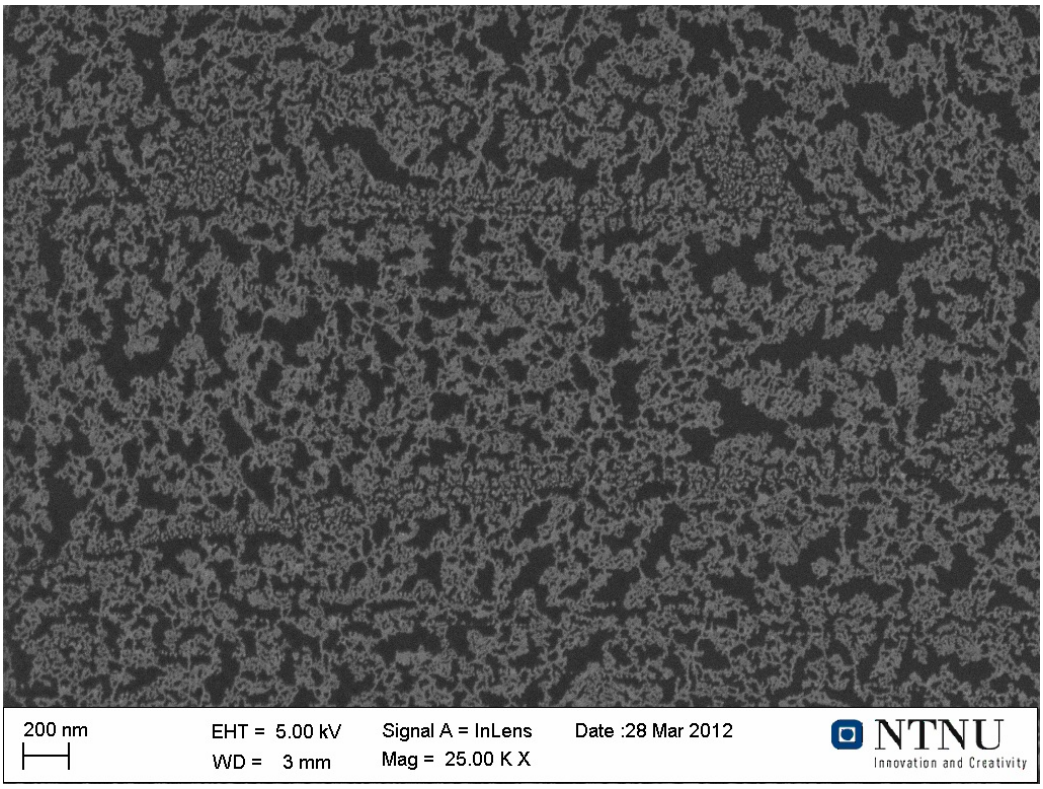

Figure 4.11: Gold evaporated onto HOPG at 150 K *for 2 minutes. Cooling the sample to* 150 K *during the gold evaporation process did not result in nice nanostructures. There are no distinct nanostructures. Sample temperatures of* 200 K *yielded similar structures. The scale can be found in the bottom left of the image.*

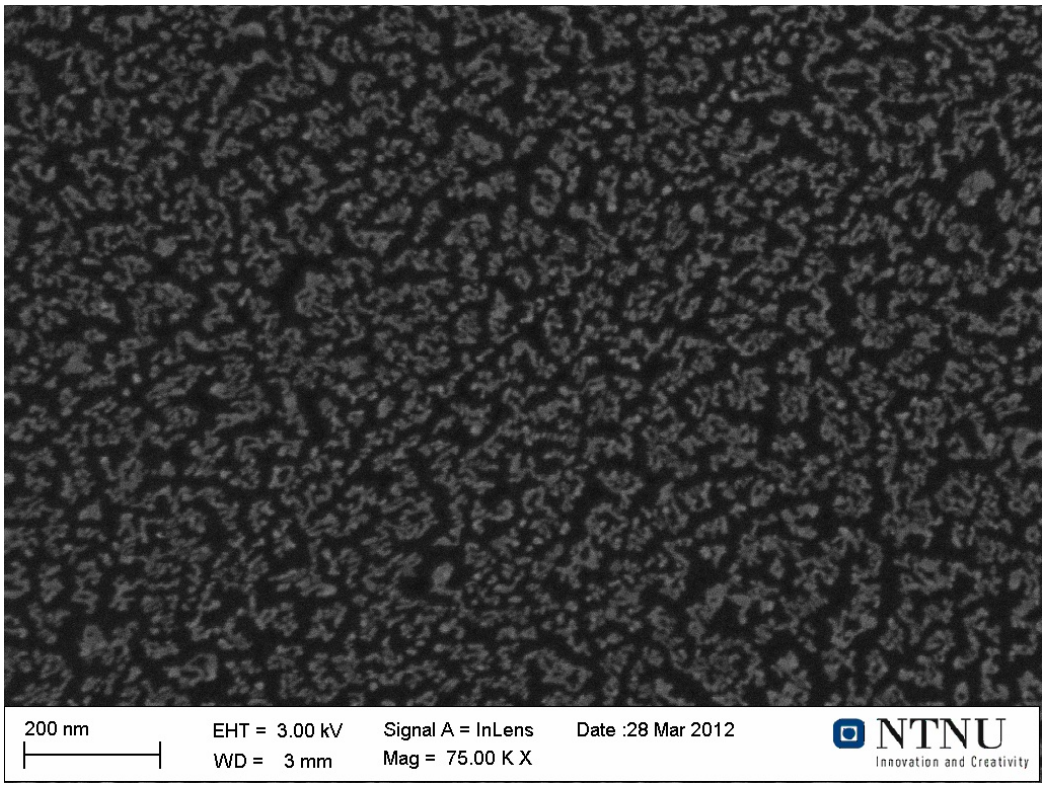

Figure 4.12: Gold evaporated onto HOPG at 250 K *for 2minutes. This SEM image from sample 13 shows the small nano-island formed by evaporation of gold onto HOPG for 2 minutes at* 250 K. *There are no dendritic structures. The scale can be seen in the bottom left of the image.*

4.2 Platinum deposited on HOPG

Figure 4.13 shows how intensity ratio of Pt over C as a function of evaporation time. The red Line is based on the original evaporation source (samples 15, 16, and 17), and the blue line is based on the new evaporation source (samples 18 through 21).

The binding energy of the Pt $4f_{7/2}$ peak as a function of intensity ratio is seen in figure 4.14. There is no clear trend of shift to higher binding energies for lower intensity ratios.

Figure 4.15 shows nanostructures on sample 18 following 3 min of evaporation (sample 18). There are small spider-like structures and some large spaghetti-like structures. The intensity ratio for this sample was $Int_{Pt}/Int_C = 0.00329$.

At an intensity ratio of $Int_{Pt}/Int_C = 0.00634$, following 6 min evaporation (sample 19), figure 4.16 shows how an increased evaporation time leads to larger structures on the surface. The structures are more complex, both the spaghetti-like structures and the island structures.

In figure 4.17 one can see that the size and complexity of the nanostructures are increasing. The intensity ratio for this sample was $Int_{Pt}/Int_C = 0.01136$ corresponding to 12 min evaporation (sample 20). The branching of the structures seem to extend further into regions that are not close to other nanostructures, and the different intensity of the white areas (the platinum) would indicate that the height of the structures is higher towards the center than at the tip of the branches. The spaghetti-like structures are still present on this sample to the same extent as on the other samples, but not in this particular image.

At an intensity ratio of $Int_{Pt}/Int_C = 0.02573$, figure 4.18 shows complex nanostructures which start to fill the entire surface of the graphite. The intensity ratio corresponds to 24 min evaporation (sample 21). The branches of the structures seem to extend further in directions away from other structures, just as in figure 4.17. The spaghetti-like structes are still present, and serve as seeds for brancing of the structures.

Figure 4.19 shows nanostructures formed after 20 min evaporation (sample 16) corresponding to an intensity ratio of $Int_{Pt}/Int_C = 0.04579$. The structures are very complex and have multiple branching. There are boundries between the different structures, indicating that the different nanostructures do not connect with each other. The different intensity of the white areas indicate an increased growth in the thickness of the structures. The spaghetti-like structures are present, with complex branched structures originating from them.

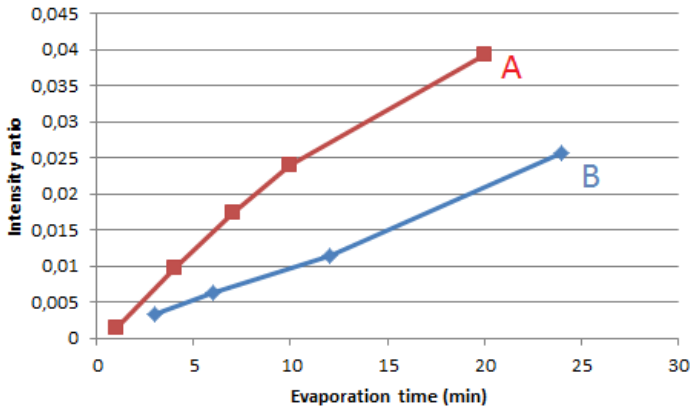

Figure 4.13: Intensity ratio of platinum over carbon as a function of evaporation time. All evaporation was performed at 9.5 A. *The red line (A) is based on data from the original platinum filament. The blue line (B) is based on data from the replaced platinum filament. Both lines shows a close to linear relationsship between intensity ratio and evaporation time.*

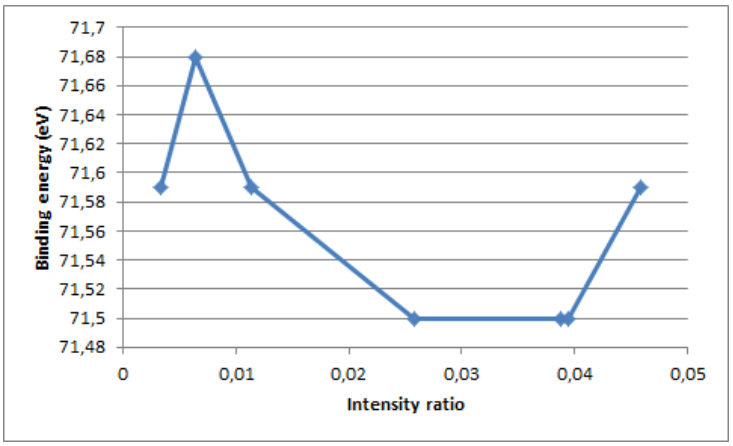

Figure 4.14: The binding energy of the Pt $4f_{7/2}$ peak as a function of intensity ratio. Only intensity ratios from evaporation with the replaced platinum source is included.

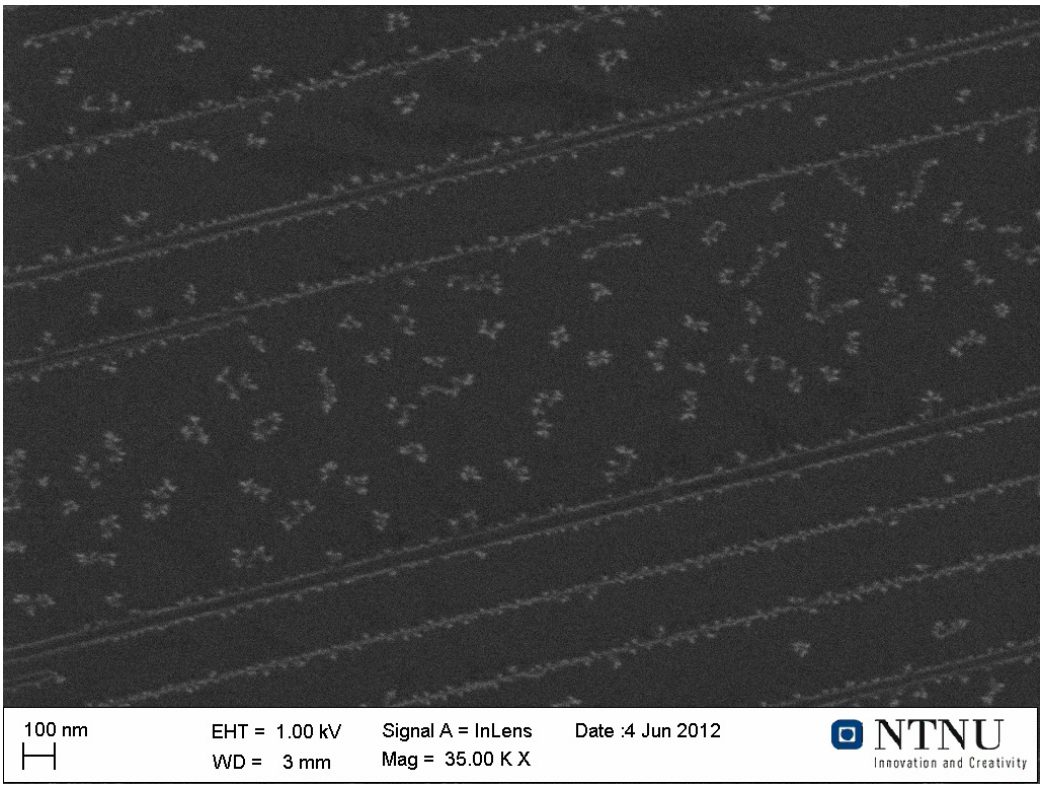

Figure 4.15: Platinum nanostructures on HOPG after 3 minutes of evaporation. This SEM image from sample 18 shows nanostructures of platinum evaporated onto graphite for 3 minutes. Spaghetti-like structures can be seen, aswell as small nano-spiders. The scale can be seen in the bottom left of the image.

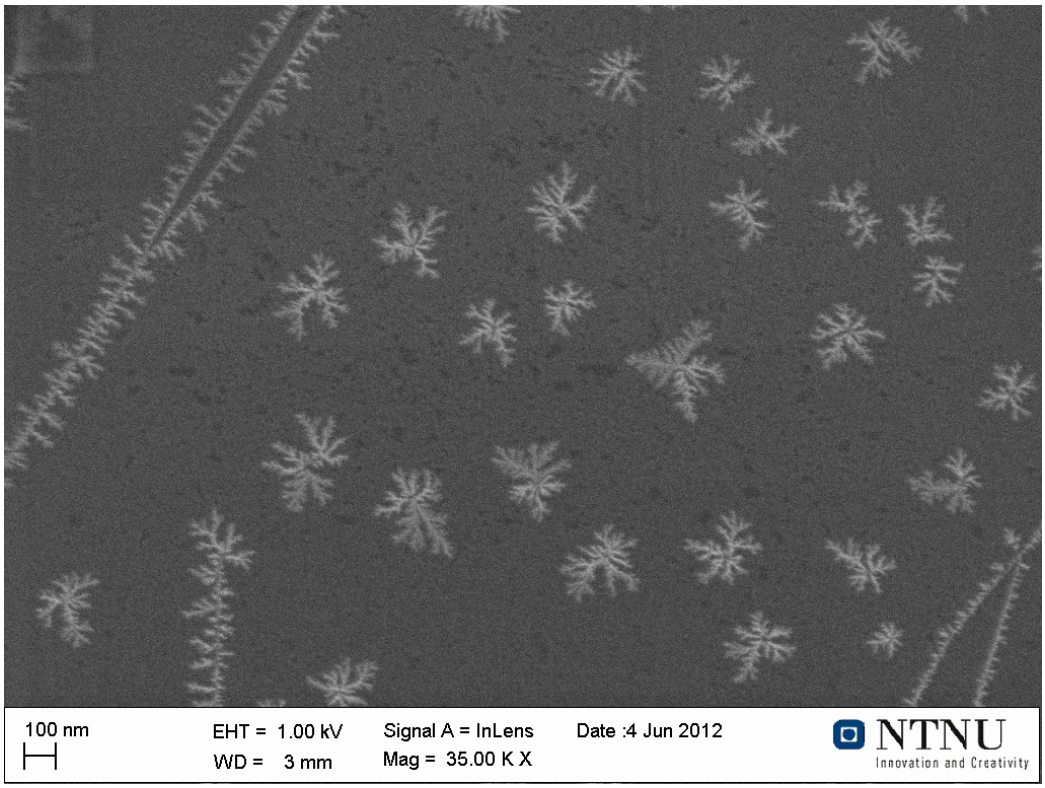

Figure 4.16: Platinum nanostructures on HOPG after 6 minutes of evaporation. This SEM image from sample 19 shows nanostructures of platinum evaporated onto graphite for 6 minutes. Spaghetti-like structures and nanoislands are present, with increased complexity as compared to figure 4.15. The scale can be seen in the bottom left of the image.

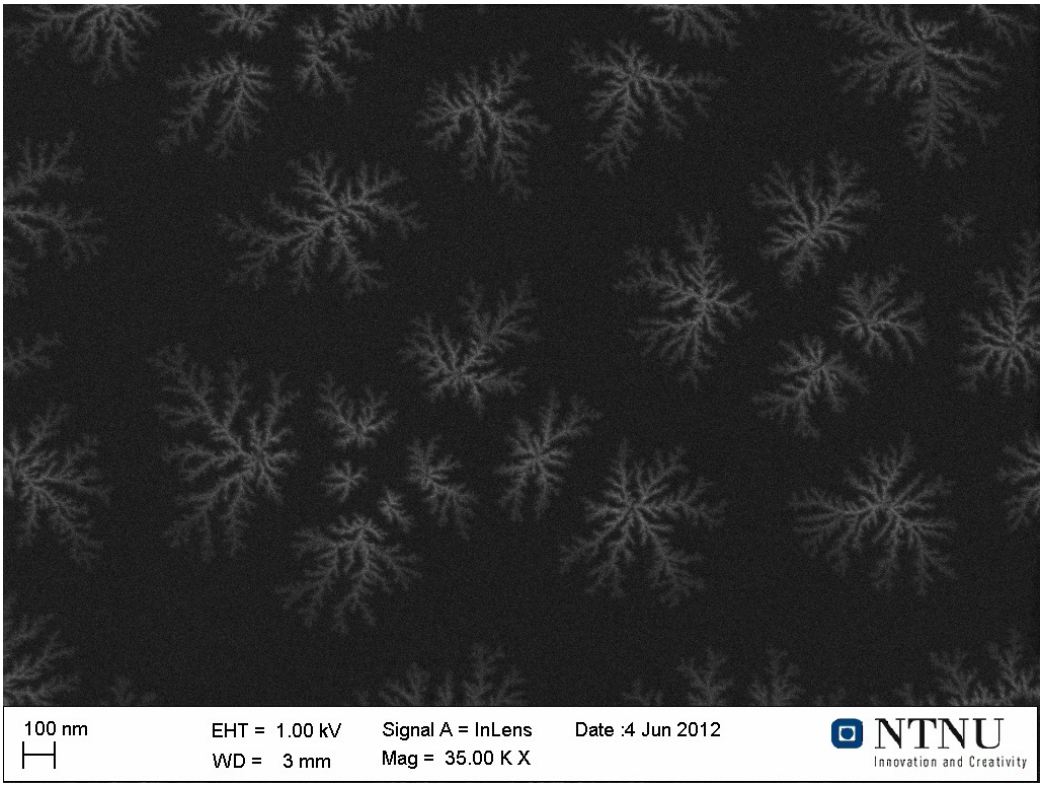

Figure 4.17: Platinum nanostructures on HOPG after 12 minutes of evaporation. This SEM image from sample 20 shows nanostructures of platinum evaporated onto graphite for 12 minutes. The nanoislands are very complex and fractal like. The different intensity of the white areas (platinum) indicate that the structures are thicker towards its center than at the edge of the branches. The scale can be seen in the bottom left of the image.

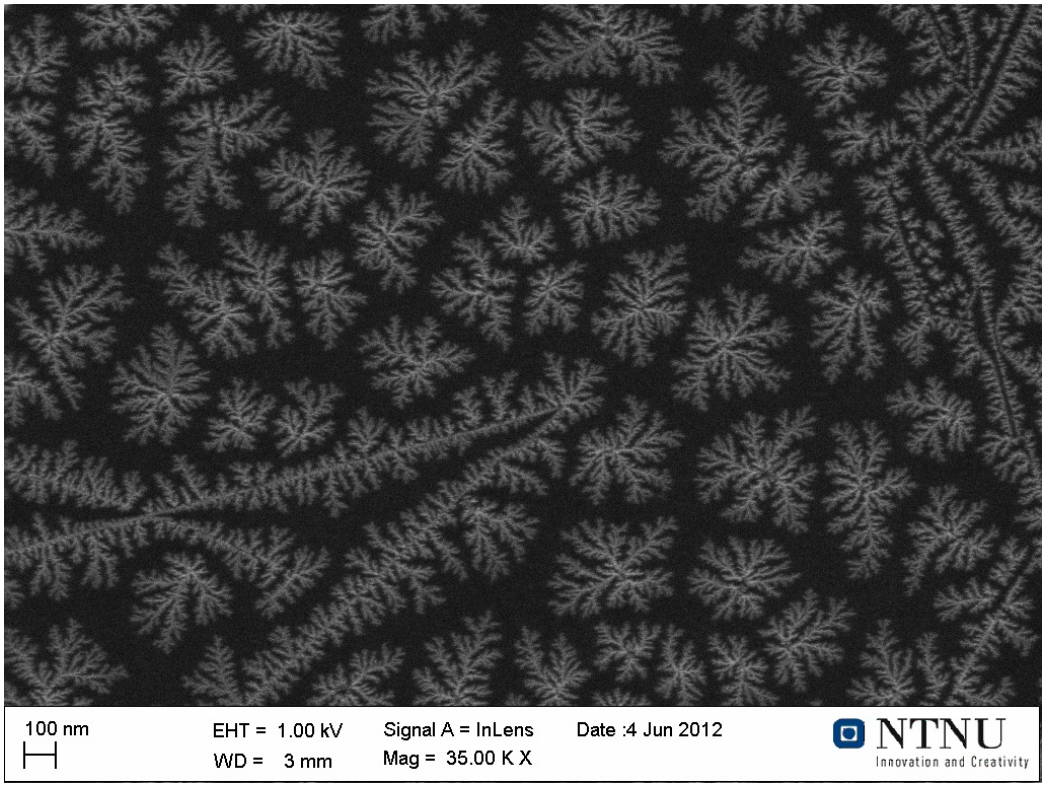

Figure 4.18: Platinum nanostructures on HOPG after 24 minutes of evaporation. This SEM image from sample 20 shows nanostructures of platinum evaporated onto graphite for 24 minutes. Spaghetti-like and fractal structures can be seen. The different intensity of the white areas (platinum) indicate that the structures are thicker at its center than at the edge of the branches. The scale can be seen in the bottom left of the image.

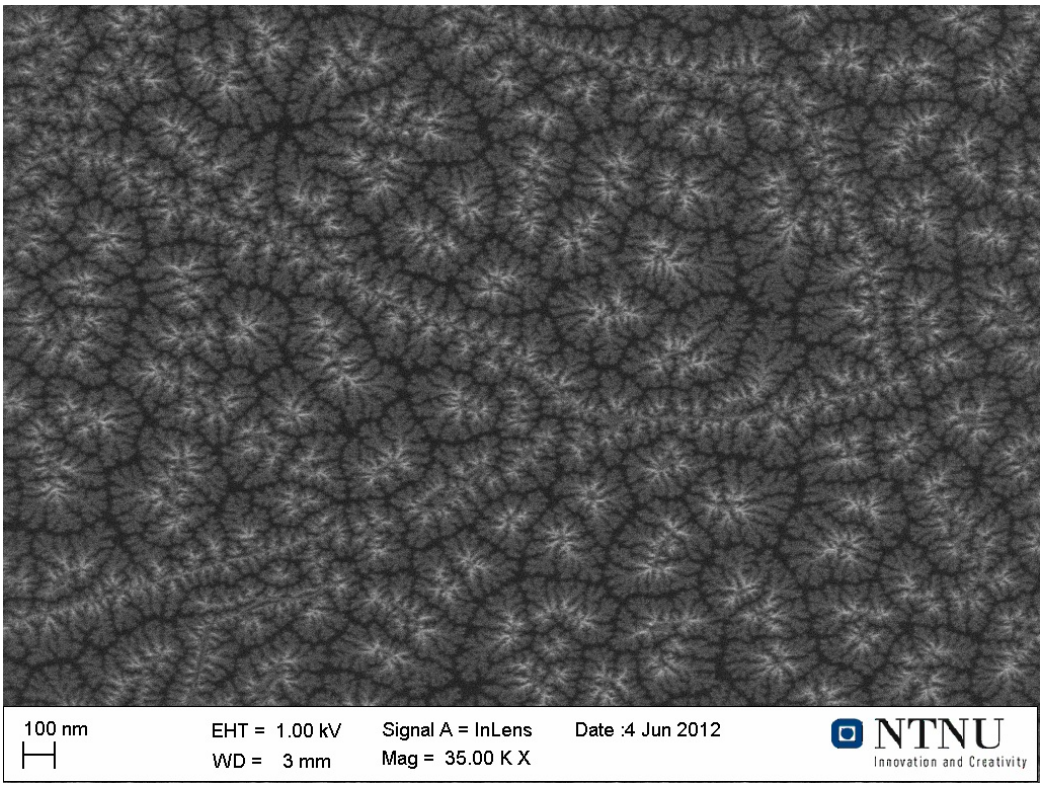

Figure 4.19: Platinum nanostructures on HOPG after 20 minutes of evaporation. This SEM image from sample 16 shows nanostructures of platinum evaporated onto graphite for 20 minutes. Spaghetti-like and fractal structures can be seen. There are clear boundries between the different nanostructures. The different intensity of the white areas (platinum) indicate that the structures are thicker at its center than at the edge of the branches. The scale can be seen in the bottom left of the image.

4.3 Oxidation of carbon monoxide over platinum

Figure 4.20 shows the current ratio of CO_2/CO as measured with QMS for sample 20 after evaporation with Pt. A, B, and C corresponds to $p_{CO}/p_{O_2} \approx 1$, $p_{CO}/p_{O_2} \approx 0.5$, and $p_{CO}/p_{O_2} \approx 2$ respectively. The pressure was adjusted manually for about 10 s between each area.

The same spectrum for samples 18,19 and 21 looked similar to figure 4.20 without any clear indication of increased or decreased oxidation of CO for any of the samples.

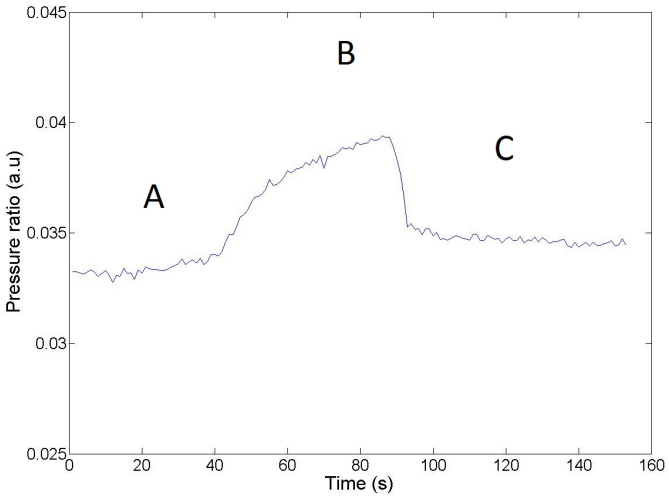

Figure 4.20: The ratio of pressure of CO_2/CO for sample 20. At A the pressure ratios of CO and O_2 are roughly equal, at B the pressure of O_2 is roughly twice that of CO, and at C the pressure of CO is roughly twice that of O_2.

Chapter 5

Discussion

SEM images of all the samples shows the presence of spaghetti-like structures on the substrate. These structures occur on all the samples and may be related to the substrate. It is believed that imperfections in the crystal structure of the HOPG are causing these structures. There may be steps between the different graphene layers of the graphite. This then causes the evaporated metals to settle at these imperfections and function as seeds for nanostructures to branch out from. This also creates barriers for the diffusion of atoms and nanoislands across the sample. Cleaving the samples with scotch tape to expose a fresh surface for evaporation has been used as method for other experiements[15, 16, 17], but does have its limitations.

Figures 4.17 and 4.18 show long branches that grow into areas where there are no other nanostructures. Incoming adatoms prefer to stick to allready growing tips, and since the area in front of the tip is empty of other structures, adatoms can diffuse toward the tip and stick. This is in correlation with diffusion limited aggregation with edge effects (section 2.4.1). Figure 4.15 shows small nano-island which are just in the critical phase were tips start to emerge.

Figure 4.5 shows how tips from gold nano-dendrites extend into areas with no other nanostructures. Also for gold the effect of tips growing in length is as would be expected from DLA with active edge diffusion. The branches are also considerably wider than monoatomic, so a classic DLA description is not accurate.

5.1 Gold deposited on HOPG

Cooling the samples down during deposition was done to see if the change in temperature (and surface mobility) would result in different nanostructures.

Earlier studies [18] has found that the dendritic structure still occur down to 170 K, however the branches become shorter and narrower at lower temperatures. Figure 4.11 shows sample 11 cooled down to 150 K. All the stuctures are connected, and do not form islands as can be seen in sample prepared at room temperature. Clear nucleation sites are also not found.

Cooling down the sample makes it adsorbe any gas that comes in contact with the surface, which was indicated with a small drop in pressure during cooling and a corresponding rise in pressure as the sample reheated to room temperature. This adsorbed gas generate many contaminants which can act as nucleation sites and reduce diffusion along the surface. It is also likely that the samples should have been degassed more thoroughly before cooling.

Figure 4.12 shows the gold nano-islands formed by evaporation onto sample 13 at 250 K. The nice dendritic structures seen in room temperature prepared samples are not seen, but neither is the connected random structure of the samples cooled to 150 K or 200 K. There are nano-island that seem to form boundries towards other islands. The large amount of islands can indicate increased amounts of contaminants on the surface. A combination of insufficient degassing and adsorbed gas due to cooling is likely to be responsible.

Activated diffusion is proportional with $e^{-\frac{E_a}{k_b T}}$ (E_a is the aktivation energy, k_b is the Boltzmann constant and T is the temperature). Thus a lower temperature gives less diffusion, which means the diffusion length will be lower and atoms will not aggregate in islands.

Table 3.1 shows that the intensity ratio of gold on carbon varied depending on current and evaporation time. For 10 min evaporation at $9,75$ A there are large variation in intensity ratio, even though all the other parameters are the same. This is most likely due to the setup of the evaporator itself. As the tungsten basket heats up it melts the gold nugget in the center. Subsequent heating (followed by cooling) of this nugget changes its geometry. The current in the tungsten wire will also transmit through the gold, and thus the geometry of the gold nugget directly affects the amount of current in the wire. So even with a constant current applied to the basket, the heat of the nugget will vary depending on the resisitive heating of the tungsten wire (which is dependant on the current through it).

Employing a significally lower or higher evaporation rate could have an impact on the gold structures formed on the surface. A very low deposition rate would reduce the atom-atom interaction during diffusion across the surface. Darby and Wayman[19] found that a higher deposition rate gave finer branches and more uniform distribution between the two types of branches. One type where secondary branches grow away from the nucleation center,

and another type where secondary branches grow towards the nucleation center. Both of these branchings are observed in this experiment, but most the type where branches grow back towards the nucleation center.

All the xps measurements of the Au 4f peak show the $4f_{7/2}$ peak to occur at 84.29 eV, except for samples 22 and 23 where the values were 84.38 eV. This would indicate that there is not an abundance of nanostructures only a few nanometers in size. The SEM images of gold structures verifies this. A shift in BE would have been caused by coloumb interaction (section 2.6) between the ejected electron and the positive charge left on the surface, but if this charge is compensated quickly enough a shift would be very difficult to observe. This is not a significant shift, and within margin of error of the analyzer. Earlier study of gold on HOPG[20] found very small shifts in the Au 4f peak in the order of 0.1 eV for small particles. There might be very small shifts for the samples, but they would not clearly be seen.

5.2 Platinum deposited on HOPG

Figures 4.15-4.19 shows how platinum nanostructures grow on HOPG for increasing intensity ratios. The transition from nano-spiders into more complex nano-fractals has been observed in earlier experiements [21] on pyrolytic graphite film. However the presence of ring-like nanostructures was not observed in this case. Julukian *et al.* [21] speculated that these structures were formed by self-assembly of nano-island formed by diffusion. Since the HOPG substrate used in these experiements showed frequent imperfections in the graphene-surface, the diffusion of entire nano-island may have been hindered.

When platinum nanostructures become sufficiently small there has previously been found a shift in the binding energy of the platinum[1, 22]. In this experiment, no such clear shift was observed. Figure 4.14 shows a trend of increased binding energy for samples 19 and 20, but sample 18 does not support this trend. The amount of spaghetti-like structures on the surface of the samples indicate that there are many imperfections in the lattice of the HOPG, and these imperfections trap more platinum. This platinum consists of thicker layers than the nano-islands and the charge left on the platinum after ejection of a photoelectron is distributed over a large enough area so that the coloumb interaction becomes negligible.

In figure 3.6 the Pt 4f peaks can be seen as the two rightmost peaks. The third peak on the left of the image is the Au $4f_{7/2}$ peak. This peak occurs at a pass energy of 200 eV, but not at 500 eV. Figure 5.1 show XPS measurements of the Au 4f peak for sample 19 at both pass energies. Both 4f peaks of gold can be seen for 200 eV. The width of the Au peaks are wide

enough that it should also be detected at a pass energy of 500 eV, indicating that there is just such a small amount of gold that it is allmost indetectable, or that there is a problem with the analyzer, detector or the software. The analyzer and detector are highly sensitive, so any problem seem very unlikely. Then there must some very small amount of gold left on the sample with a very distinct peak with very small width that at a pass energy of 500 eV the signal drowns in the background.

A total of 10 HOPG substrates were available for use during the experiements, and so they had to be reused at least once. Scotch tape was used twice to remove two layers of graphite as well as any metal still left on the surface. The removed layers were not transparent to light and therefore atleast several micrometer thick. This should be sufficient to remove any gold on the sample from previous experiments, but a small amount may have migrated into the sample at imperfections of the substrate lattice.

5.3 Oxidation of carbon monoxide over platinum

There were no clear results to be gained from the study of CO oxidation over platinum nanostructures.

By measuring the amount of CO_2 formed by oxidation of CO close to the surface of the sample, the goal was to see if the shape of the platinum nanostructures would lead to an increase in the turnover rate of the platinum. There were no clear indication of any change in reactivity.

This experiment was performed by varying the pressure of oxygen in the chamber, with te pressure of carbon monoxide remaining constant. Measurements should also have been performed where oxygen was introduced at about 10^{-7} torr and the pressure of carbon monoxide was varied.

The studies were all performed using the same sample holder in all cases, and the temperature was kept constant at room temperature (310 K). By performing the measurements at various temperature, one would be able to find the temperature dependance of the catalytic processs, and hopefully find the nanostructures which resulted in the lowest temperature for the process. A viable large scale way of producing low temperature platinum catalyst using less platinum would have a great commercial value.

By mixing the carbon monoxide and oxygen at a precise ratio before introducing the gases to the chamber, it would be much easier to measure any change in the amount of carbon dioxide from sample to sample. By

using precise manometers* when mixing the gases, one would be able to have a well-defined pressure ratio of carbon monoxide and oxygen which can be reproduced for each measurement. If all other parameters are also kept constant throughout the experiments, then any change in amount of carbon dioxide over the sample would be due to the sample surface itself. The differentially pumped QMS would be able to detect very small changes in the partial pressures.

5.4 Future experiments

Cleaving the HOPG samples in a vacuum would increase the cleanliness of the surfaces. Allthough cleaving the sample in air and then degassing in a vacuum for sufficient time will generate nice surfaces, cleaving the sample in a vacuum after degassing would generate the purest surface for evaporation. Darby and Wayman[19] found that air-cleaved graphite would leave a high amount of particles on the surface with nondescript shapes. Similar to the ones obtained on samples 11,12 and 13. Vaccum-cleaved samples would however leave evaporation to form dendritic branches similar to the ones found on the samples prepared at room temperature. This shows that air-cleaving and degassing in a vacuum can generate clean surfaces, a system of cleaving the system in a vacuum would be better to ensure clean surfaces.

A temperature programmed desorption (TPD) of carbon monoxide from the sample surface would also have given information about the catalytic properties of the platinum nanostructures. This has been performed by Julukian[1] which found a correlation between decreased smaller particle size and lowered desorption temperature for platinum on pyrolytic graphite. With a HOPG substrate, this effect should be even more clear, as there would be larger uniform areas.

*instrument used to measure pressure

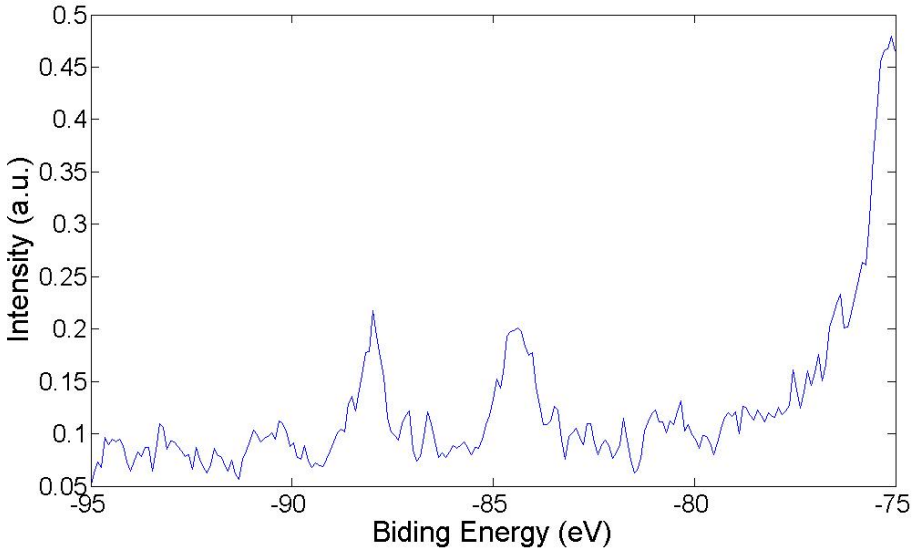

(a) 200 eV *pass energy*

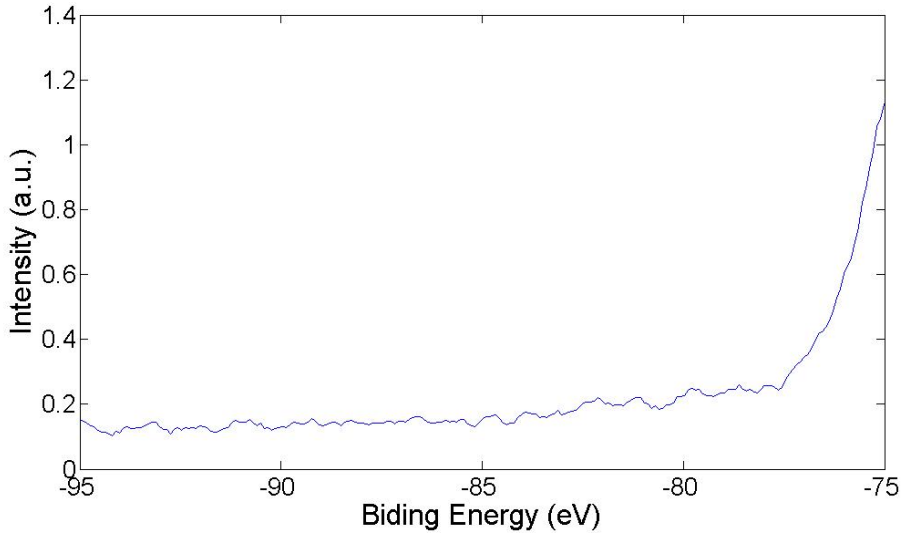

(b) 500 eV *pass energy*

Figure 5.1: XPS measurement of the Au 4f peak on sample 19 with a pass energy of (a) 200 eV *and (b)* 500 eV*. The rightmost peak in both figures is the Pt* $4f_{5/2}$ *peak. (a) shows that with a pass energy of* 200 eV *a small amount of gold is detected within the top few nanometers of the sample, which is not seen in (b) at* 500 eV*.*

Chapter 6

Conclusion

Gold evaporated onto HOPG at room temperature formed nano-dendrites and spaghetti-like structures on the surface. The formation of the dendrites is in agreement with previous research, but the spaghetti is believed to be formed by imperfections and contaminants. For gold evaporated at reduced temperatures, no such dendritic structures were found.

Platinum evaporated onto HOPG at room temperature formed nano-spiders at low deposition amount and more complex fractal structures at higher deposition rates, which is in agreement with previous studies. No significant shift in binding energy was observed as a function of intensity ratio, which is not in agreement with previous studies.

Studying the oxidation of CO over the surface of the platinum covered HOPG yielded no clear corrolation between particle size and oxidation rate.

Bibliography

[1] A. Julukian, S. Raaen, T. Fadnes, and M. Balci, "Size effect on thermal desorption of CO from Pt nanostructures on graphite," 2011. http://link.aip.org/link/doi/10.1063/1.3596572.

[2] N. N. Greenwood and A. Earnshaw, *Chemistry of the Elements*. Elsevier, 2nd ed., 1997. http://www.knovel.com/web/portal/browse/display?_EXT_KNOVEL_DISPLAY_bookid=402&VerticalID=0.

[3] H. Baker and H. Okamoto, *ASM Handbook, Volume 3 - Alloy Phase Diagrams*. ASM Iinternational, 1992. http://www.knovel.com/web/portal/browse/display?_EXT_KNOVEL_DISPLAY_bookid=3107&VerticalID=0.

[4] T. Janssens, B. Clausen, B. Hvolbaek, H. Falsig, C. Christensen, T. Bligaard, and J. Norskov, "Insights into the reactivity of supported Au nanoparticles: combining theory and experiments," *Topics in Catalysis*, vol. 44, no. 1-2, pp. 15–26, 2007. http://www.ingentaconnect.com/content/klu/toca/2007/00000044/F0020001/00000335.

[5] S. Schroder and M. Gottfried, "Temperature-Programmed Desorption (TPD)," 2002. http://userpage.chemie.fu-berlin.de/~pcprakt/tds.pdf.

[6] J. H. Moore, C. C. Davis, M. A. Coplan, and S. C. Greer, *Building Scientific Apparatus*. Cambrigde University Press, 4th ed., 2009. http://www.knovel.com/web/portal/browse/display?_EXT_KNOVEL_DISPLAY_bookid=3151&VerticalID=0.

[7] C. Brundle, C. A. J. Evans, and S. Wilson, *Encyclopedia of materials characterization - Surfaces, interfaces, thin films*. Butterworth-Heinemann, 1992. http://www.knovel.com/web/portal/browse/display?_EXT_KNOVEL_DISPLAY_bookid=714&VerticalID=0.

[8] B. V. Crist, *Handbook of monochromatic XPS spectra - The elements and native oxides*. John Wiley & sons ltd., 2000.

[9] L. Scudiero, "Homepage of Louis Scudiero, Washington State University," http://public.wsu.edu/~scudiero/.

[10] T. A. Witten and L. M. Sander, "Diffusion-limited aggregation," *Phys. Rev. B*, vol. 27, pp. 5686–5697, May 1983. http://link.aps.org/doi/10.1103/PhysRevB.27.5686.

[11] H. Röder, K. Bromann, H. Brune, and K. Kern, "Diffusion-Limited Aggregation with Active Edge Diffusion," *Phys. Rev. Lett.*, vol. 74, pp. 3217–3220, Apr 1995. http://link.aps.org/doi/10.1103/PhysRevLett.74.3217.

[12] S. E. Van Bramer, "An Introduction to Mass Spectrometry," 1997. http://science.widener.edu/svb/massspec/massspec.pdf.

[13] G. K. Wertheim, S. B. DiCenzo, and S. E. Youngquist, "Unit Charge on Supported Gold Clusters in Photoemission Final State," *Phys. Rev. Lett.*, vol. 51, pp. 2310–2313, Dec 1983. http://link.aps.org/doi/10.1103/PhysRevLett.51.2310.

[14] K. Mills and J. R. Davis, *ASM Handbook, Volume 12 - Fractography*. ASM international, 1987. http://www.knovel.com/web/portal/browse/display?_EXT_KNOVEL_DISPLAY_bookid=3116&VerticalID=0.

[15] R. Anton and I. Schneidereit, "*In situ* TEM investigations of dendritic growth of Au particles on HOPG," *Phys. Rev. B*, vol. 58, pp. 13874–13881, Nov 1998. http://link.aps.org/doi/10.1103/PhysRevB.58.13874.

[16] D. C. Lim, I. Lopez-Salido, R. Dietsche, M. Bubek, and Y. D. Kim, "Oxidation of Au nanoparticles on HOPG using atomic oxygen," *"Surface Science*, vol. 600, no. 3, pp. 507 – 513, 2006. http://www.sciencedirect.com/science/article/pii/S0039602805012380.

[17] H. Hövel, T. Becker, A. Bettac, B. Reihl, M. Tschudy, and E. Williams, "Crystalline structure and orientation of gold clusters grown in preformed nanometer-sized pits," *Applied Surface Science*, vol. 115, no. 2, pp. 124 – 127, 1997. http://www.sciencedirect.com/science/article/pii/S0169433297801948.

[18] C. Wayman and T. Darby, "Nucleation and growth of gold films on graphite: II. The effect of substrate temperature," *Journal of Crystal Growth*, vol. 28, no. 1, pp. 53 – 67, 1975. http://www.sciencedirect.com/science/article/pii/0022024875900263.

[19] T. Darby and C. Wayman, "Nucleation and growth of gold films on graphite: I. Effects of substrate condition and evaporation rate," *Journal of Crystal Growth*, vol. 28, no. 1, pp. 41 – 52, 1975. http://www.sciencedirect.com/science/article/pii/0022024875900251.

[20] I. Lopez-Salido, D. C. Lim, R. Dietsche, N. Bertram, and Y. D. Kim, "Electronic and Geometric Properties of Au Nanoparticles on Highly Ordered Pyrolytic Graphite (HOPG) Studied Using X-ray Photoelectron Spectroscopy (XPS) and Scanning Tunneling Microscopy (STM)," *The Journal of Physical Chemistry B*, vol. 110, no. 3, pp. 1128–1136, 2006. http://pubs.acs.org/doi/abs/10.1021/jp054790g.

[21] A. Julukian and S. Raaen, "Formation of Pt nanostructes on graphite and transition from nano-spiders to nano-flakes," unpublished.

[22] P. Marcus and C. Hinnen, "XPS study of the early stages of deposition of Ni, Cu and Pt on HOPG," *Surface Science*, vol. 392, no. 1–3, pp. 134 – 142, 1997. http://www.sciencedirect.com/science/article/pii/S0039602897005372.

List of Figures

List of Tables